UNIVERSIDAD DE CONCEPCIÓN
FACULTAD DE CIENCIAS FÍSICAS Y MATEMÁTICAS
PROGRAMA DE MAGÍSTER EN ASTRONOMÍA

SEARCHING FOR A PREDICTED METALLICITY VARIATION IN THE TYPE II GLOBULAR CLUSTER NGC 362

(BUSCANDO UNA VARIACIÓN DE METALICIDAD PREDICHA EN EL CÚMULO GLOBULAR DE TIPO II NGC 362)

Profesor Guía: Dr. Sandro Villanova
Departamento de Astronomía
Facultad de Ciencias Físicas y Matemáticas
Universidad de Concepción

Tesis para ser presentada a la Dirección de Postgrado de la Universidad de Concepción para optar al grado de Magíster en Astronomía

CAROLINA ALEJANDRA VARGAS GONZÁLEZ
Concepción - Chile
Julio 2021

To my family

ACKNOWLEDGEMENTS

Quiero agradecer profundamente a mi compañero de carrera, amigo, novio y ahora esposo, quien estuvo siempre a mi lado y me apoyó cuando más lo necesitaba. Por tu confianza, lealtad y sincero amor te estaré infinitamente agradecida, *Matías Eduardo Sotomayor Webar*.

Deseo también agradecer a mi familia, principalmente a mi madre Erika González, quien es mi pilar fundamental y la persona que me lo ha dado todo desde mi primer día de vida; a mi padre Marcelo Vargas, quien me inspiró el amor por la Astronomía; a mi hermana Camila Vargas y a su hermosa hija Bianca, quienes amo incondicionalmente; a mi hermano Gustavo Vargas y a su pequeña bebé Agustina; a mi amada princesa Mía Margarita y a mi pequeña Pelusita; y por último a mis abuelos Maigo y Pepe, simplemente los mejores abuelos que podría desear.

Finalmente pero no menos importante, quiero agradecer a mis profesores Sandro Villanova y Douglas Geisler, quienes me educaron a lo largo de mi carrera y también me ayudaron y guiaron en la elaboración de mi primer paper y tesis.

Carolina Vargas G.

Abstract

According to Milone et al. (2017), NGC 362 is a rare Type II Galactic globular cluster, showing a complex pseudo two-color diagram or 'Chromosome Map' based on their HST UV Legacy photometry. The clear separation of its stellar populations in the color-magnitude diagram and the distribution of the giant stars in the chromosome map strongly suggests that NGC 362 could host stars with both cluster-nominal as well as enhanced heavy-element abundances, in particular iron, leading to an intrinsic metallicity spread, as shown by at least some other Type II globulars. However, despite previous spectroscopic observations of NGC 362, no such metallicity variation has been detected, but previous studies did not pre-select potential normal and anomalous stars. Our main goal is to search for any internal variation of [Fe/H] which would give us insight into the formation and evolution of this interesting globular cluster and Type II clusters in general. In this work, we present the abundance analysis for a sample of 11 red giant branch members based on high-resolution and high S/N spectra obtained with the MIKE echelle spectrograph mounted at the Magellan-Clay telescope. The stars were carefully selected from the HST photometry to maximize the possibility of including a metallicity variation based on the Milone et al. (2017) scenario. HST and GAIA photometry and astrometry has been used to determine atmospheric parameters and membership. We obtained T_{eff}, log(g) and v_t for our target stars and measured the mean iron content of the sample and its dispersion with three different methods, which lead to $[Fe/H]_1$=-1.10±0.02, $[Fe/H]_2$=-1.09±0.01 and $[Fe/H]_3$=-1.10±0.01, while the internal dispersion turned out to be $\sigma_{[Fe/H]_1}$=0.06±0.01, $\sigma_{[Fe/H]_2}$=0.03±0.01 and $\sigma_{[Fe/H]_3}$=0.05±0.01 respectively. The error analysis gives an internal dispersion due to observational error of 0.05 dex. Comparing the observed dispersion with the internal errors, we conclude that NGC 362 does not show any trace of an internal iron spread, in particular between the anomalous red stars with presumably higher metallicities and the bulk of the stars that fall along the nominal first and second generation sequences, based on the chromosome map. Thus, our findings do not support the metallicity spread predicted by Milone et al. (2017). This makes NGC 362 the first Type II cluster which definitely does not show such a spread, thus requiring a modification to their prediction.

Keywords – Globular Cluster: NGC 362 - Stars: Abundances.

Contents

List of Tables

List of Figures

Chapter 1

Introduction and Context

1.1 Overview of Globular Clusters

Globular Clusters (GCs) are vast and dense aggregates of gravitationally bound stars that are packed in a roughly spherical distribution. Most GCs have masses $\gtrsim 10^4 M_\odot$ and ages $\gtrsim 6$ Gyr (Kharchenko et al., 2013), with typically 10^4-10^6 members stars, all located at virtually the same distance from us. Distributed mainly in the halo surrounding the Milky Way's galactic plane, as well as in the Galactic bulge and disk, these stellar objects are among the oldest known in the universe, furthermore they are bright and present in large numbers in our Galaxy as well as other massive galaxies, allowing us to observe them at large distances, as well as to progress in our understanding of stellar evolution and in a variety of fundamental astrophysical problems.

As of 2010, the Milky Way has over 150 cataloged GCs (Harris 1996, 2010 edition) and possibly many more undiscovered. The recent large-scale surveys in the near- and mid- infrared wavelengths such as the VISTA Variables in Vía Láctea (VVV) (Minniti et al., 2010; Saito, R. K. et al., 2012) have made good progress studying the bulge and an adjacent section of the mid-plane where the star formation activity and the extinction from interstellar dust are high, increasing very significantly the number of candidate GCs.

Figure 1.1: The Galactic Globular Cluster NGC 362 observed by the Hubble Space Telescope. Image Credit: Hubble WFC3, NASA, ESA, J. Heyl, I. Caiazzo, & Javiera Parada (UBC).

1.1.1 Abundance Variations

Not long ago, GCs were traditionally considered Simple Stellar Populations (SSPs) (Renzini and Buzzoni, 1986), with all of the stars having the same age, distance and initial chemical composition. However, it has now become clear that they are not as simple as initially thought. The intensive scrutiny of GCs over the last decade has lead to the discovery of Multiple Stellar Populations (MSPs) within them, indicating an intrinsic range in their present composition which is evidenced by both spectroscopic and photometric methods.

Through high-resolution spectra in particular we can detect intracluster chemical variations in light elements, most notably C, N, O, Na, Mg and Al (Carretta et al., 2009). These star-to-star variations display (anti)correlations, best evidenced by a Na-O anticorrelation (see Figure 1.2), and point to the likely presence of different generations of stars, formed in more than a single burst. The first generation (1G) of stars have primordial chemical composition, where stars are O rich and Na poor, the same as typical field stars of the same metallicity, while the second generation (2G) of stars are born in a medium chemically enriched by the earlier generation(s), resulting in enhanced He, N, Al and Na abundances and depleted C and O.

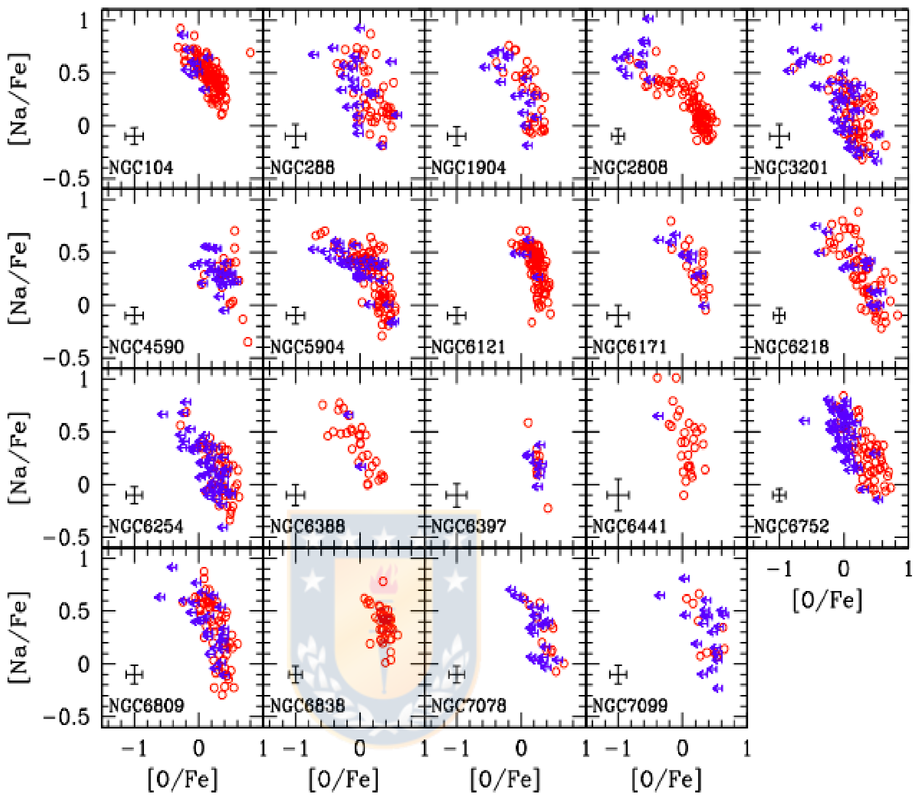

Figure 1.2: The Na-O anticorrelations observed by Carretta et al. (2009) in 19 GCs from GIRAFFE and UVES high-resolution spectra. Star-to-star error bars are marked in each panel. The arrows indicate the upper limits of O abundances, while detections are represented as open circles.

1.1.2 Polluter Candidates

The chemical signature of GCs suggests that multiple generations of stars are formed from gas polluted by the products of hot proton-capture processes which take place in the interiors of the 1G of asymptotic giant branch (AGB) stars (D'Antona et al., 2002), fast rotating massive main sequence (MS) stars (Decressin et al., 2007) and/or massive binaries (de Mink et al., 2009), which eventually reach the surface and then escape via stellar winds. The GC potential well is able to retain this gas and eventually leads to the subsequent formation of chemically enriched 2G stars (D'Ercole et al., 2008).

As mentioned above, three stellar types have been mainly proposed as possible polluters since they are able to reach extreme temperatures within their interiors. Concerning the nucleosynthesis, it is clear that polluted candidates must be He-enriched, since this element is the main outcome of H-burning. According to constraints provided by observational evidence, polluter stars must be able to:

1. Modify only the light elements (e.g., C, N, O, Na, Mg, and Al) without contributing heavy elements such as Fe.

2. Acquire a mechanism to bring the processed material from the core (or H-burning shell) to the stellar surface (e.g., through the convection process for AGB stars and by rotational mixing for fast rotating massive stars (FRMS)).

3. Have a way to release the processed material into the intra-cluster medium (ICM) with a slow enough velocity that prevents the material from escaping the globular cluster potential well (e.g., slow AGB winds and slow mechanical equatorial winds for FRMS).

1.1.2.1 Intermediate-mass AGB stars

D'Antona et al. (2002) proposed intermediate-mass AGB stars as polluter candidates from which the next generations formed. The hydrogen burning shell of AGB stars more massive than ∼3-4 $M_\odot$ with temperatures between 6-10$\times 10^7$ K can extend into the convective envelope through the hot bottom burning (HBB) process, allowing a significant nucleosynthesis to take place and affecting directly the envelope composition of the star by H-burning (e.g., by the CNO cycle and by the NeNa and MgAl chains, see Figure 1.3). The second dredge-up (SDU) experienced by ∼ 3-8 $M_\odot$ stars leads to a considerable He enrichment in the whole stellar envelope (Becker and Iben (1979); Ventura et al. (2002); Renzini (2008)), and according to the AGB scenario, the CNONa anomalies would arise when the star experienced the HBB process, which is able to prevent the formation of carbon stars (AGB stars whose atmosphere contains more carbon than oxygen) even when the third dredge-up (TDU) occurs (Renzini and Voli, 1981). As the star evolves, the mass loss via slow winds of AGB stars could be retained by the GC from which the next generation CN-strong and Na-rich stars formed (Thoul et al. (2002); D'Ercole et al. (2008); Renzini (2008)). Eventually, star formation ceases by supernovae (SNe) events which sweep the gas and the nucleosynthesis' products from the cluster. However, we note that AGB models cannot reproduce the abundances pattern (see Carretta et al. (2009)) found in GC stars, in particular AGB stars are not able to reproduce the O-depletion observed in some extreme GC stars ([O/Fe] < -0.5 dex; Ventura and D'Antona (2009)).

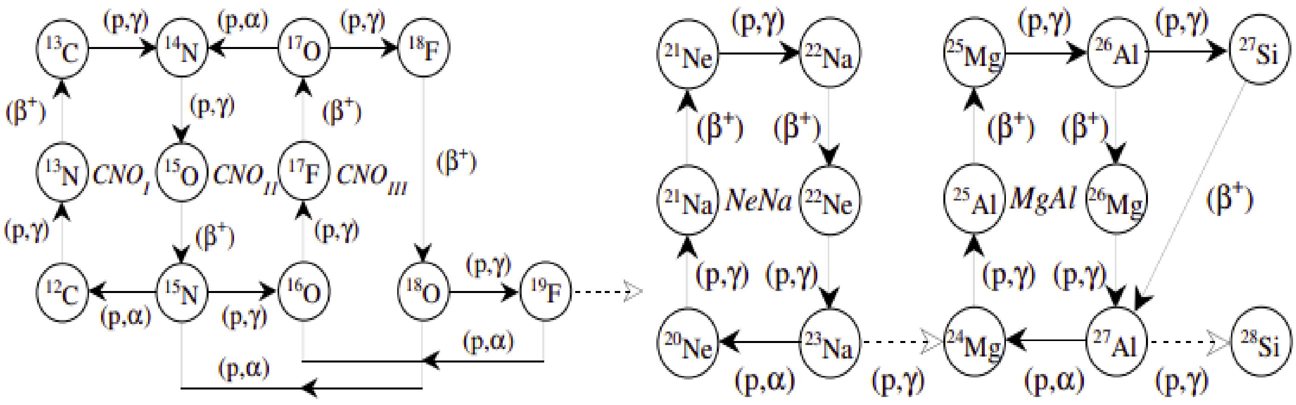

Figure 1.3: Proton-capture reactions through the CNO cycle (activated at $T \sim 20$ MK) and the NeNa and MgAl-chains (activated at $T \sim 40$ MK and $T \sim 70$ MK, respectively) from Arnould et al. (1999). The dashed line represents the possible leakage out of the cycles.

1.1.2.2 Fast rotating massive stars

Decressin et al. (2007) developed a scenario where they suggest that winds produced by FRMS are responsible for providing the enriched material from which the next stellar generations formed. The fast rotation of FRMS removes the material from the stellar surface and then insert it in the interstellar medium (ISM) at low velocities. Additionally, it leads to the internal mixing of H-burning products, which are synthesized in the convective core of the star and then brought to the stellar surface. At high enough velocities, the initial rotation of FRMS yield the formation of equatorial gas disks around them, which loses mass with velocities lower than 50 km s^{-1}, allowing the GC potential well to retain this gas. According to this scenario, the ejecta of FRMS are mixed with pristine gas to form the next stellar generation in the vicinity of their massive progenitors, with a range of yields depending on the mass and rotation rate. We however note that this model is also not able to reproduce the exact pattern of the observed abundances.

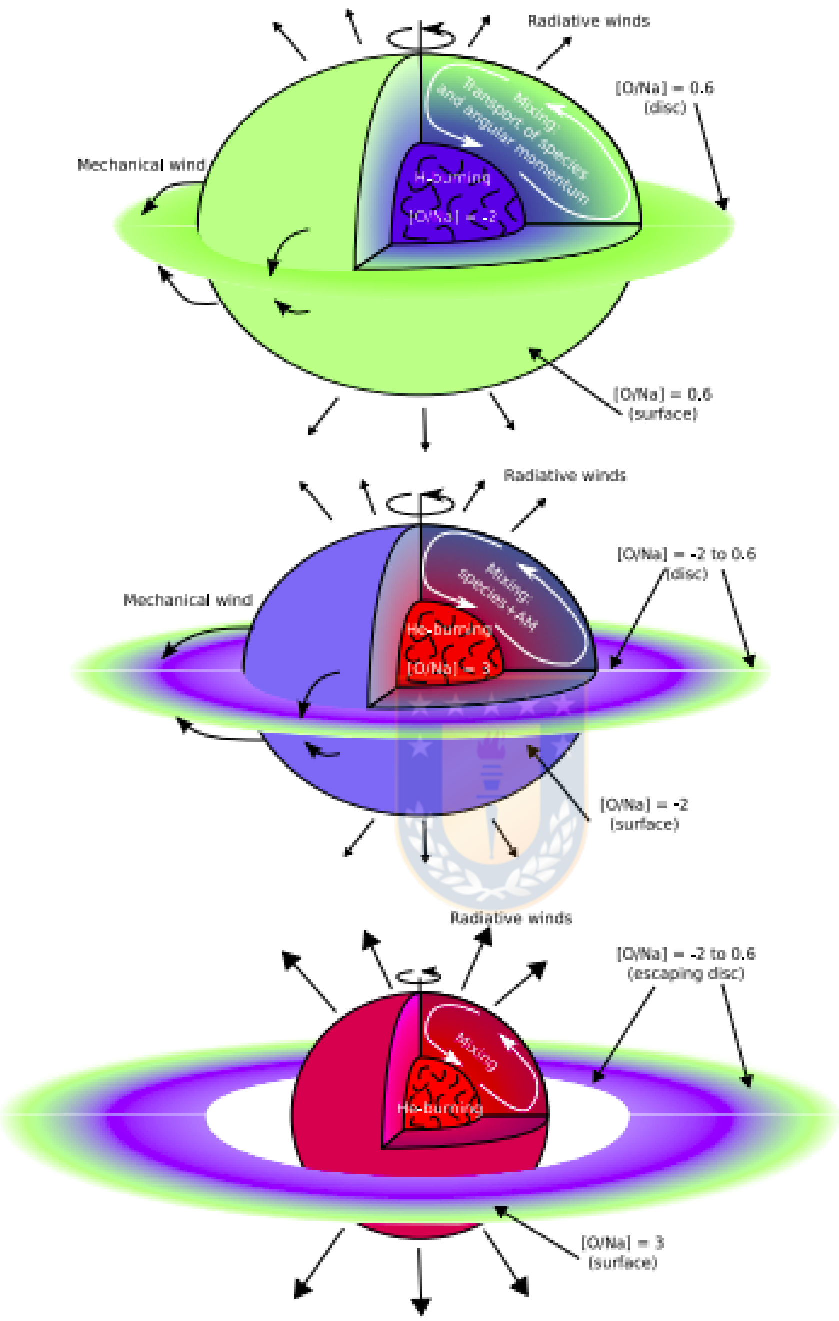

Figure 1.4: Sketch of the evolution of a FRMS by Decressin et al. (2007). The colors represent the chemical composition of the stellar regions and of the disc. Top: During the MS, a slow outflowing equatorial disc forms and dominates matter ejection with respect to radiative winds. Middle: At the beginning of He-burning, the composition of the disc material spans the range in [O/Na] observed today in low-mass cluster stars. The star has already lost an important fraction of its initial mass. Bottom: Due to heavy mass loss, the star moves away from critical velocity and does not supply its disc anymore; radiatively-driven fast wind takes over before the products of He-burning reach the stellar surface.

1.1.2.3 Massive Binaries

de Mink et al. (2009) propose massive binaries as source for the internal pollution of GCs, which are expected to be members of interacting binary systems. The authors showed that there may be more polluted material ejected by massive binaries than by slow winds of intermediate-mass AGB stars and FRMS. Assuming masses of 20 and 15 $M_{\odot}$ for the two stars, and low initial rotation rates, we can neglect the effect of rotationally induced mixing on the low-velocity ejecta, and follow the evolution from the start of H-burning until central carbon burning. Shortly after the H runs out in the center, the primary star expands and starts to transfer mass to its companion, which efficiently accretes all the transferred mass and associated angular momentum. When the companion star accretes $\sim 1.5\ M_{\odot}$ it approaches critical rotation and consequently the majority of the transferred mass is ejected from the system. After the mass transfer of nearly the entire envelope, the donor star contracts and ignites helium, becoming a Wolf-Rayet star. At this point, a second phase of mass transfer occurs when the Wolf-Rayet star expands during He-shell burning, but this time $\sim 1.0\ M_{\odot}$ is accreted by the secondary star and then ejected by its rotationally enhanced wind. After that, the primary star ignites carbon and fills its Roche lobe to finally explode as a supernova.

One of the main hurdles of all the previously proposed self-enrichment scenarios is ***'the mass budget problem'***. The observations (e.g., Smith and Norris 1982; Carretta et al. 2009) show that the primordial population observed in GCs is much less than the enriched population formed by ejecta of its massive stars. The number of 2G stars can not not be explained by the processed material from 1G stars because there are not enough ejecta to create a 2G which is equally numerous as the 1G. Assuming a standard Kroupa (2001) IMF, the total mass of AGB ejecta is only 1-10% of the total GC mass (Bekki and Norris, 2006); while for slow winds of FRMS, it provides only $\sim$ 10% of the total number of low-mass stars (Decressin et al., 2007). Thus, the possible polluters cannot be fully established yet and no current scenario is able to completely reproduce the complex behavior of MSPs (Renzini et al., 2015).

The iron abundance homogeneity found in most GCs studied to date tells us that supernovae events cannot be responsible for the chemically enriched medium from which the NG formed. Although GCs are able to retain the gas from stellar winds, leading to MSPs, they are generally not massive enough to retain the Fe-peak elements produced by supernovae ejecta (Willman and Strader, 2012). There are some exceptions, such as ω Centauri and Terzan 5, that display an intrinsic dispersion in Fe of ~ 1 dex. Nonetheless, these objects are now classified as the remnant core of a tidally disrupted dwarf galaxy accreted by the Milky Way (Majewski et al., 2000) and as a Galactic bulge primordial building block (Ferraro et al., 2009), respectively. We can also find a few traditional GCs with highly debated iron spreads in the literature, such as M22 (Marino et al., 2011a; Mucciarelli et al., 2015). However the origin of these unusual clusters is even less clear than that of the more common ones that only show light element, and no heavy element, variations.

1.1.3 MSPs seen through CMDs

The complexity of MSPs can also be very well characterized photometrically by using a combination of ultraviolet (UV) and optical Hubble Space Telescope (HST) photometry. The F275W, F336W and F438W filters, also known as the 'Magic Trio', of the HST UV and Visual Channel of the Wide Field Camera 3 (WFC3/UVIS) are very sensitive to OH, NH, CN and CH molecular bands and hence do an excellent job of separating MSPs in appropriate color-color and color-magnitude diagrams (CMDs) (Piotto et al., 2015) (see Figure 1.5). Milone et al. (2017) found a method to maximize this separation through the construction of 'Chromosome Maps' (see Figure 1.6); these pseudo two-color diagrams make use of the magic trio and of the F814W filter to produce a significant split of different stellar populations. By using high-precision photometry of red giant branch (RGB) stars in 57 GCs from The HST UV Legacy Survey of Galactic GCs (Piotto et al., 2015; Milone et al., 2017), Milone et al. found a surprising variety of MSP behavior for each cluster, all of them displaying distinct distributions. Based on their chromosome maps, the authors were able to identify certain generic patterns and define two classes of GCs: Type I clusters show the typical bimodality where the 1G and 2G of stars are almost always clearly separated and no other strong pattern emerges, whereas Type II GCs display more complex chromosome maps, with 1G and/or 2G sequences that appear to be split, with an additional distribution of very red stars. A detailed analysis of their HST photometry of Type II clusters exposed that sub-giant branches (SGBs) are split in UV-optical CMDs with a (less populated) fainter SGB joining onto a redder RGB (see Figure 1.7), while the SGBs of Type I clusters split only in the chromosome map. Further spectroscopic analysis revealed that stars in the faint SGB and red RGB belonging to well studied Type II clusters are enhanced in iron, global

C+N+O content, and generally, in s-process elements compared to stars on the normal, bluer RGB, whereas Type I clusters host populations that show only light element variations (Milone et al., 2017). Hence, these Type II GCs display intrinsic variations in these elements, in particular Fe, meaning they possess a metallicity spread.

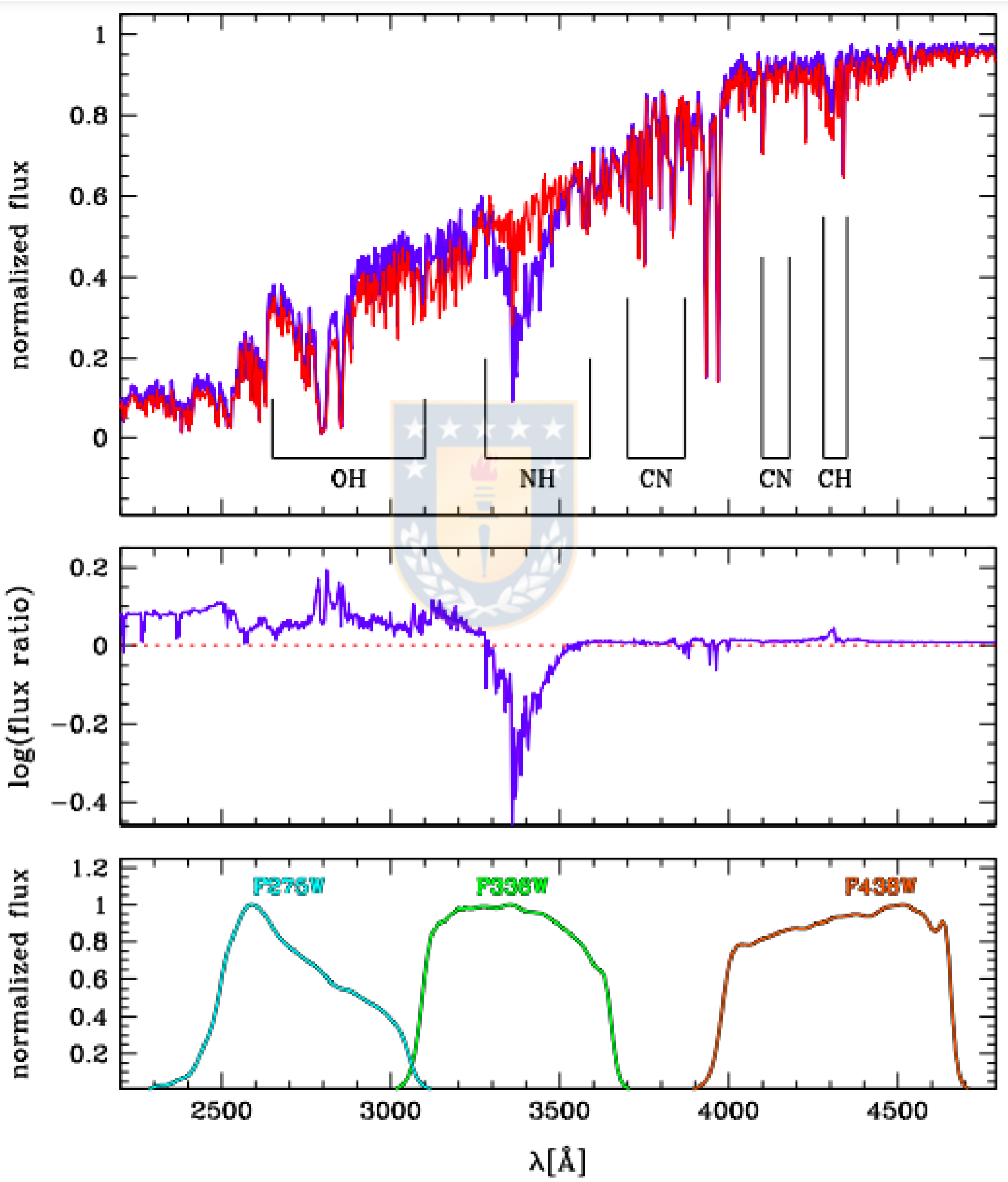

Figure 1.5: Upper panel: Simulated spectrum of 1G (red) and 2G (blue) stars, with a number of molecular absorption bands labeled. Middle panel: Flux ratio between the two simulated spectra from the upper panel. Lower panel: Bandpasses of WFC3/UVIS filters with F275W, F336W and F438W used in photometric studies to uncover MSPs. The figure was taken from Piotto et al. (2015).

Iron is the most tightly bound nucleus in nature with a binding energy of 8.8 MeV per nucleon, and therefore the heaviest element that can be synthesized by the fusion of lighter nuclei in massive stars (Dwek, 2016). Fe has been extensively studied in almost all astrophysical contexts due to the huge number of available atomic transitions over the whole spectral range, and it is primarily produced in Type II supernovae (SNe II) events which show clear signs of hydrogen in their spectra. The progenitors of core-collapse SN are very often found to be members of close binary systems and are also believed to spend most of their lives as early-B- and O-type stars. The presence of a wide metallicity range found in some GCs demands that they were massive enough to retain SN ejecta, allowing for multiple bursts of star formation, with each generation becoming progressively enriched in Fe (e.g., Bedin et al. 2004).

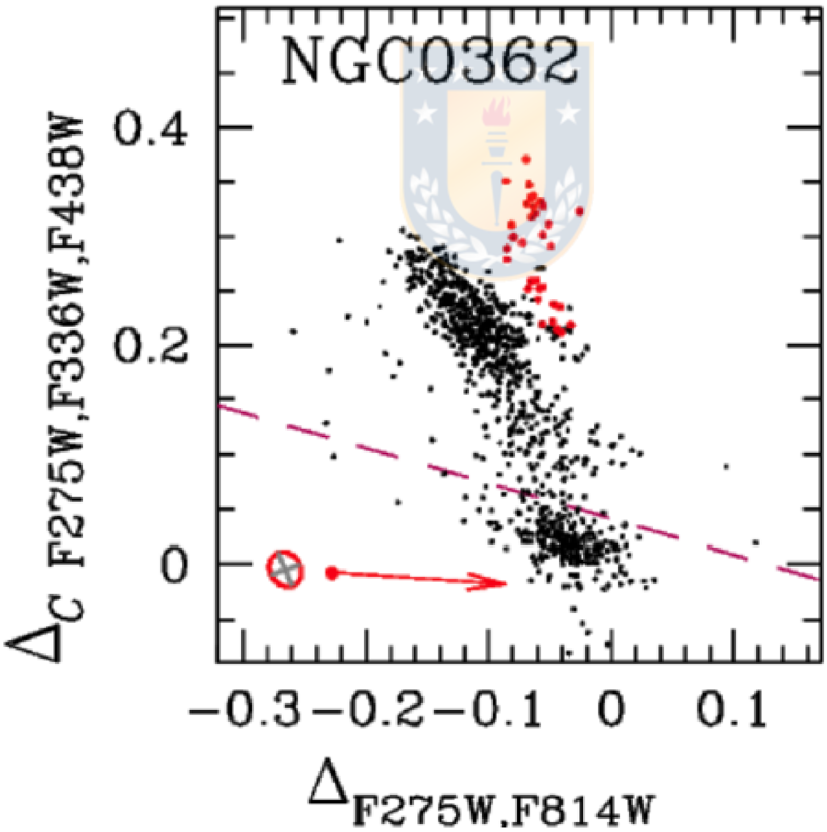

Figure 1.6: HST pseudo two-color diagram or 'Chromosome Map' of the Type II GC NGC 362 by Milone et al. (2017), showing photometric errors (red ellipse), separation of 1G (lower) and 2G (upper) stars and remaining stars that fall redward of these sequences (red), making it Type II GC.

Chromosome maps have proven to be an efficient tool to identify candidate GCs with internal variations of heavy elements, which are until now very rare and their study essential for understanding GC formation and evolution. All the known clusters with a significant iron spread like ω Centauri belong to Type II, nonetheless there are several clusters in this category that are currently not known to have Fe abundance spreads. However, previous studies have not specifically targeted samples of stars believed to best show such a spread based on their chromosome map. In this work we present a detailed chemical study of the Type II GC NGC 362 in order to search for any intrinsic Fe variation. The evident split of 1G and 2G sequences with a significant distribution of red stars in the Chromosome Map (see Figure 1.6), leading to its Type II classification, strongly argues that NGC 362 should have an intrinsic metallicity spread. Milone et al. (2017) estimate that this cluster could host up to 10% of stars having an iron content higher than the main population and the Fe spread could be of the order of 0.1-0.2 dex. Usually metallicity variations are associated with massive GCs; however, NGC 362 has an intermediate mass of $3.45 \times 10^5 M_\odot$ (Baumgardt and Hilker, 2018). Therefore, if an Fe spread is confirmed, it will help us to constrain formation scenarios, as well as the lower limit to the mass of a GC required to retain supernovae ejecta. For this purpose, we collected high-resolution spectra for 11 RGB member stars taken with the MIKE spectrograph, selected to cover a wide range in the chromosome map and CMDs to include stars predicted to have a metallicity spread. This data has been complemented with HST and GAIA photometry to fully characterize the atmospheric parameters and confirm or reject the hypothesis of the presence of an iron spread, as the chromosome map suggests.

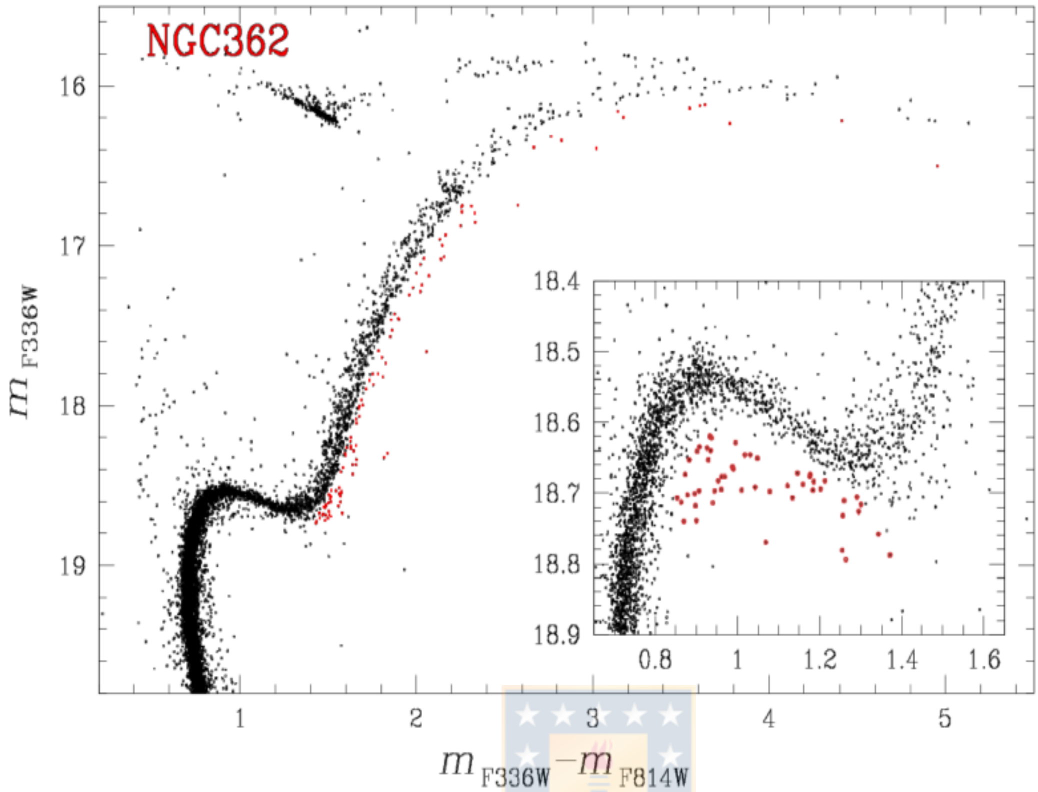

Figure 1.7: HST F336W-F814W CMD of NGC 362 by Milone et al. (2017). The red stars in Figure 1.6 are also marked red here. Note that they fall to the red and faintward of the main RGB and SGB loci. These stars should have enhanced Fe compared to the stars in the main loci, according to their scenario.

1.2 Chemical Abundances Determinations

The two most powerful and widely-used spectroscopic methods to determine chemical abundances and atmospheric parameters of a star are Equivalent Widths (EQWs) and Spectral Synthesis:

1.2.1 Equivalent Width Method

In a plot of intensity (I) versus wavelength (λ) (see Figure 1.8), the EQW (W_λ) of an absorption line (a) corresponds to the measure of the width of a rectangle (b) having the height of the normalized continuum intensity level, measured from the base at zero flux, whose area is equal to the area of the spectral line. This method can be applied to either emission or absorption lines to measure the strength of spectral features and finally get abundances.

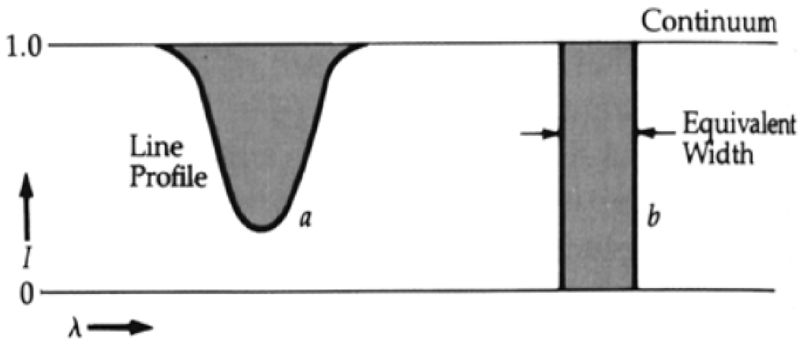

Figure 1.8: Representation of EQW method of an absorption line.

Formally, the EQW is given by the equation:

$$W_\lambda = \int_{\lambda_1}^{\lambda 2} \left(1 - \frac{F_\lambda}{F_0}\right) d\lambda$$

where F_λ is the intensity across the wavelength range between λ_1 and λ_2, and F_0 represents the continuum intensity of the spectral line.

In practice, the typical code we use to determine the chemical composition of a star is MOOG (Sneden, 1973). A standard MOOG running option called *abfind* force-fits abundances of different elements to yield computed EQWs that agree with observed ones previously measured with other software packages. In Figure 1.9 we show an example of EQW measure for an iron line (element 26) of a RGB star with the MOOG program.

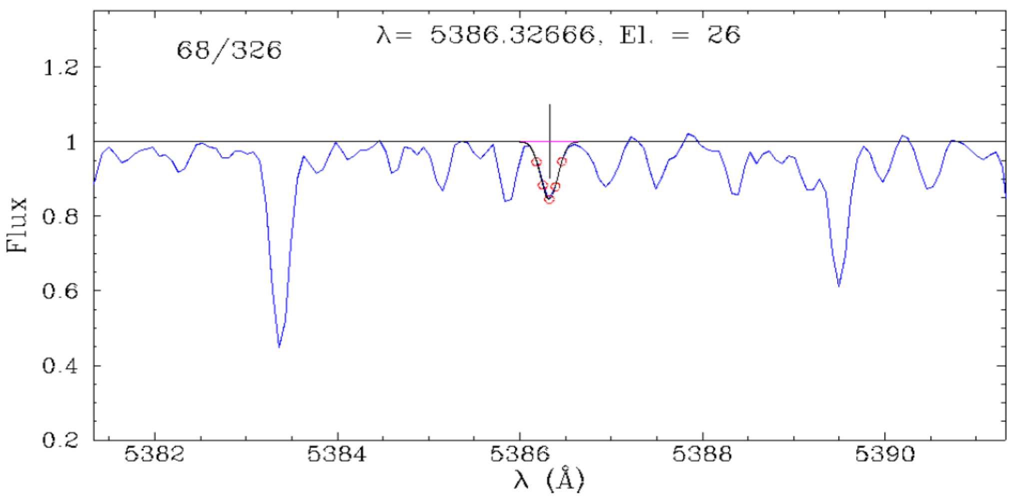

Figure 1.9: Example of EQW measure for an iron line for one of our RGB member star with the MOOG code. Red symbols mark the best fit of the absorption line.

1.2.2 Spectral Synthesis Method

The other standard technique to get chemical abundances from the spectra is the Spectral Synthesis method. This method is suitable for low signal-to-noise (S/N) and/or limited wavelength range data, and requires the atmospheric parameters effective temperature, T_{eff}, and surface gravity, log(g), of the star to be known. It computes a set of synthetic spectra that we compare and manually match to the observed spectrum, allowing us to get an estimate of the chemical abundances with high accuracy. In Figure 1.10 we show an example of synthetic spectra and their comparison to an observed spectrum.

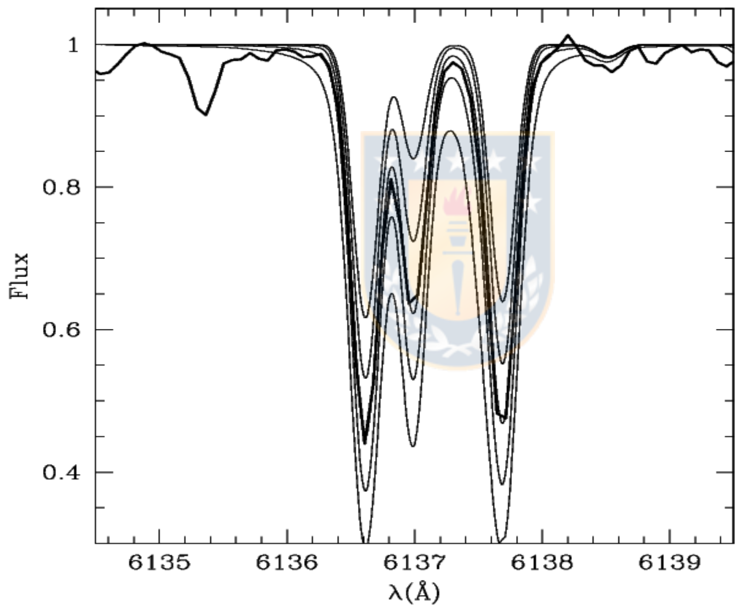

Figure 1.10: Example of the strong Fe band at 6137 Å used as Fe indicator, from one of our target RGB stars. The observed spectrum is represented by the thick line and overplotted are four synthetic spectra that we used to determine Fe abundances. Synthetic spectra were calculated with an abundance of -0.50, -0.25, 0.00, +0.25 and +0.50 dex with respect to the [Fe/H] content we estimated for the star (See Section 4.2).

Chapter 2

Target Selection

2.1 Maximizing the possibility to detect an Iron Spread

As we explained in Chapter 1, the MSP phenomenon can be seen through photometry using an appropriate combination of UV and optical HST filters. To achieve our main goal of testing for the presence of an iron spread in the Type II galactic GC NGC 362 we maximized the possibility to detect such a putative spread by separating and comparing different generation of stars, as judged by the HST photometry. In Figure 2.1 we show our target selection to study the NGC 362 cluster that was observed in November 2018 with the MIKE spectrograph. In the upper panel of the figure we plotted the CMD of the cluster with the RGB separated in three different color regimes in order to maximize the possibility to detect an intrinsic metallicity variation. The red branch contains the red stars from the chromosome map (see Figure 1.6) that are presumed to have higher metallicities according to the Milone et al. (2017) scenario, while the blue and green branches contain the normal 1G and 2G stars which are presumed to have normal metallicities. In the lower panels of the figure we show the finding charts with the three separate RGB stars overplotted (blue, green and red) from the upper panel.

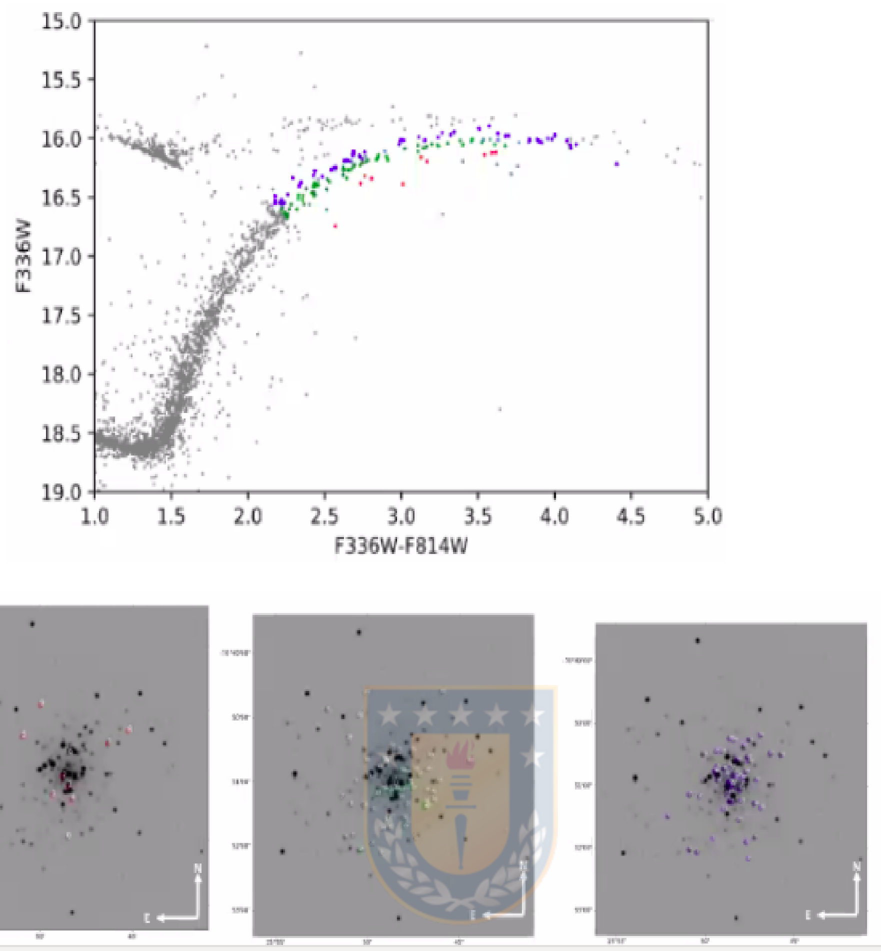

Figure 2.1: Target selection of NGC 362. Upper panel: The CMD of the cluster from HST photometry with the upper RGB separated into three color regimes: blue, green and red. Lower panels: Finding charts of NGC 362 with each colored and separated RGB stars from the top diagram. Red RGB stars are overplotted in the lower left panel, while the green and blue RGB stars are shown in the middle and in the lower right panels respectively.

We also reproduced the chromosome map of NGC 362. To do this, we used the F275W, F336W, F438W and F814W magnitudes from The HST UV Legacy Survey (Piotto et al., 2015; Milone et al., 2017) and formed the two pseudo-colors ΔF275W,F814W and ΔCF275W,F336W,F438W. Our reproduced chromosome map is plotted in Figure 2.2 and clearly shows the dominant presence of typical 1G and 2G stars (black points), as well as the anomalous redder stars, which are the same stars falling along the redder part of the RGB in the CMD.

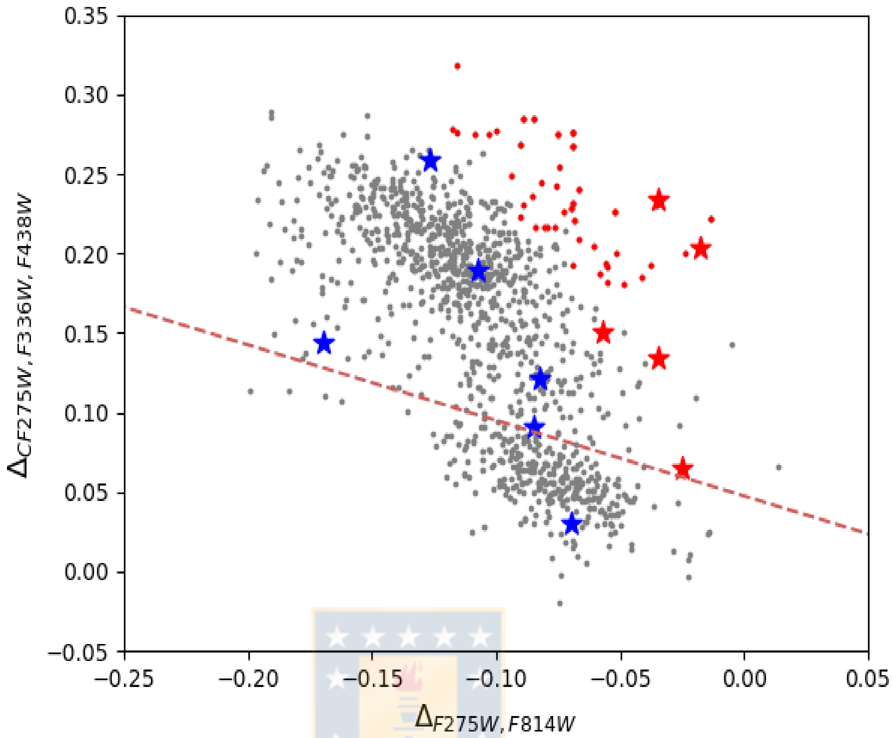

Figure 2.2: Chromosome map of NGC 362. Our targets are represented as red (anomalous) and blue (normal) filled stars. The magenta dashed line is used to separate 1G from 2G stars and the red points indicate the red-RGB stars according to the definition of Milone et al. (2017).

We then plotted the F336W vs. (F336-F814W) CMD (see Figure 2.3) with our 11 observed RGB member stars. This plot shows a main as well as a loosely populated redder RGB that connects to a fainter SGB. Following the method presented in Milone et al. (2017), we plot in red stars in this CMD which lie along the reddest RGB (which merges with the faint SGB), and mark these same stars as red in the chromosome map (see Figure 2.2). These red stars fall to redder ΔF275W,F814W colors of the main locus of 2G stars. These outliers (hereby anomalous stars) were identified by Milone et al. (2017) and led to their classification of NGC 362 as a Type II GC. These anomalous stars presumably have a higher metallicity than the bulk of the stars that fall along the nominal 1G and 2G sequences (hereby normal stars), according to their scenario. Thus, we need to observe as many of these anomalous stars as possible, along with a similar number of normal (metallicity) 1G/2G stars, in order to optimize the possibility of detecting any putative metallicity spread between them (Marino et al., 2018).

Our final targets included the brightest anomalous stars from the chromosome map along with bright normal stars chosen from the CMD which lay along the bluer/brighter RGB (avoiding the green stars in Figure 2.1), in order to maximize the possibility to detect any variation in iron spread.

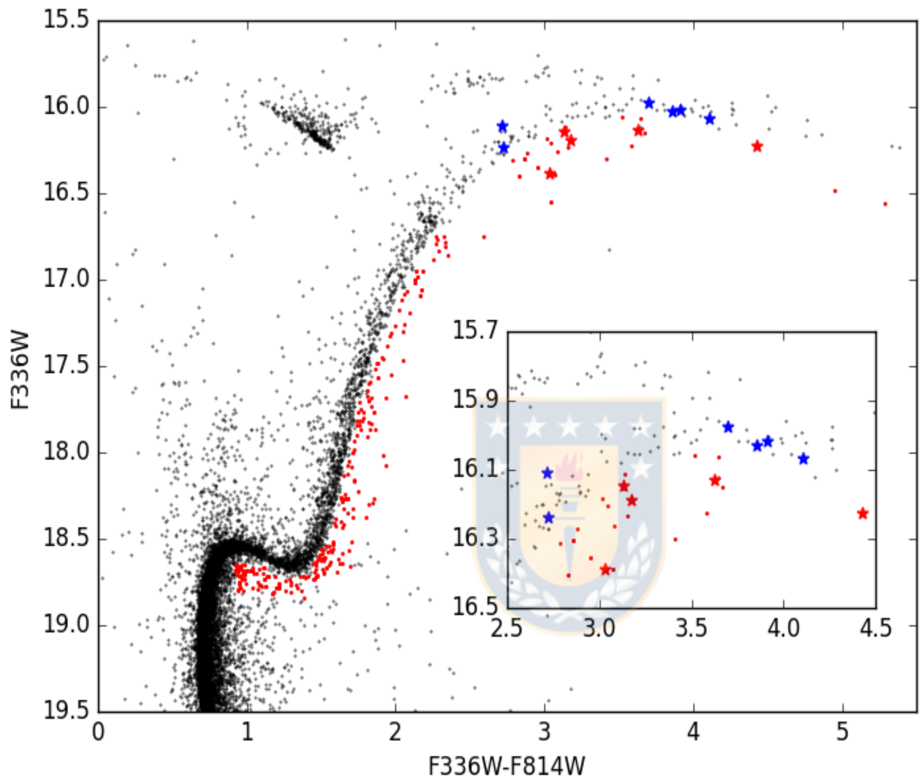

Figure 2.3: The CMD of NGC 362 from the HUGS catalogue (Nardiello et al., 2018; Piotto et al., 2015) with the eleven observed RGB members indicated as blue and red filled stars. Blue targets are presumed to have normal metallicities, while red targets should have higher metallicities according to the Milone et al. (2017) scenario.

Chapter 3

Observations and Data Reduction

3.1 Observations and Data Management

Twelve candidate NGC 362 members, six normal and six anomalous stars (as judged by their position in HST color-magnitude and color-color diagrams, as described above), were observed during the nights of November 8th and 9th 2018 with the MIKE high-resolution spectrograph (Bernstein et al., 2003) mounted at the Magellan-II/Clay telescope of the Las Campanas Observatory (Chile). The spectra cover the range 3350-5000 Å and 4850-9400 Å in the blue and the red arms, respectively. A 0.7″ slit was used for the observations, corresponding to a spectral resolution of R=53000 and R=42000 in the blue and the red arms, respectively. Stars were observed using either 2×900s (stars #11, 12, 13, 17, 18, 19, 20) or 3×1200s (stars #14, 15, 16, 21, 22) exposures. The signal-to-noise (S/N) is between 57 and 105 around 6000 Å. Data were reduced using the CarPy pipeline[1] (Kelson et al., 2000; Kelson, 2003) and included overscan subtraction, flat fielding, order extraction, wavelength calibration and sky subtraction. Milky flat fields were taken with the aid of a diffuser to correct for the pixel to pixel variations. Spectral rectification was performed using *continuum* and *sarith* tasks in IRAF [2]. We also used the *scombine* package to combine all the spectra per star and the *fxcor* package to measure radial velocities using a synthetic spectrum as a template. Observed radial velocities were converted to the heliocentric system leading to a mean value of $RV_{helio} = 221.87 \pm 1.95$km s^{-1}, which is in good

[1] https://code.obs.carnegiescience.edu/mike

[2] IRAF is distributed by the National Optical Astronomy Observatory, which is operated by the Association of Universities for Research in Astronomy, Inc., under cooperative agreement with the National Science Foundation.

agreement with Harris (1996) and Baumgardt et al. (2019) who found values of $RV_H = 223.50 \pm 0.5\text{km s}^{-1}$ and $RV_B = 223.26 \pm 0.28\text{km s}^{-1}$ respectively. Thus, this is a first strong indication, apart from their location in the various CMDs, that our targets are all indeed members of NGC 362.

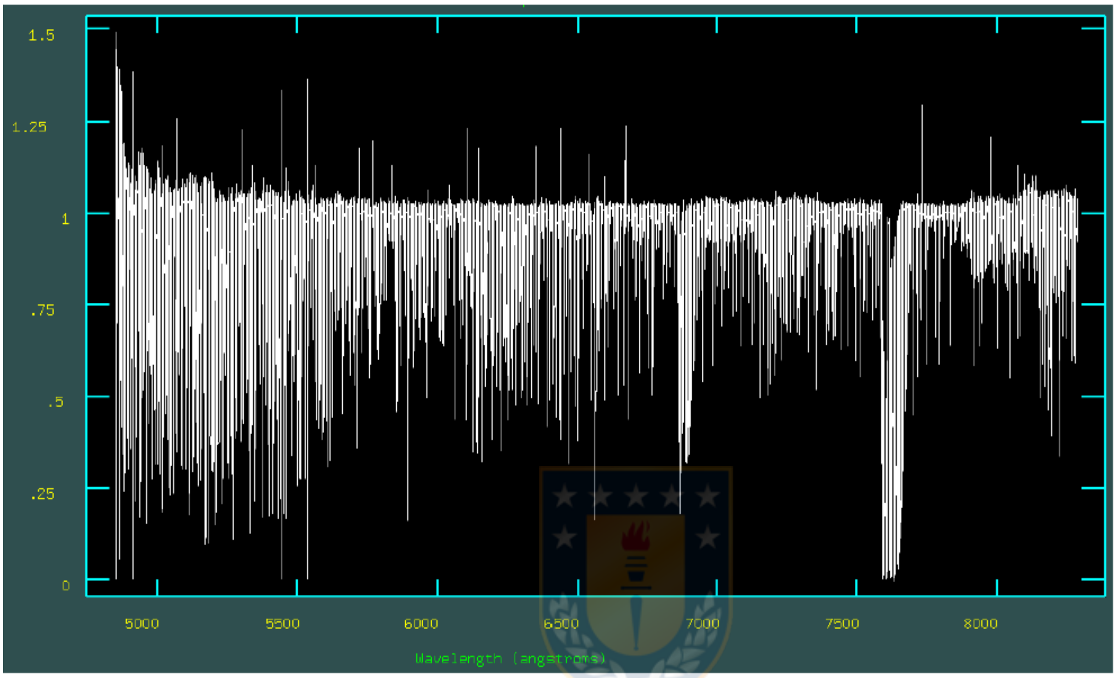

Figure 3.1: Example of a reduced high-resolution spectrum for a RGB star from NGC 362.

3.2 Proper Motions in the field of NGC 362

In order to further confirm the membership of our targets, we plot the proper motions of our stars around the cluster, making use of GAIA eDR3 survey (Collaboration et al., 2020). Figure 3.2 shows in cyan the most likely cluster members while our targets are indicated with red and blue filled stars. We considered as likely members those stars within a radius of 0.6 mas/year around the center of the cluster. It is clear from this figure that one of our targets (star number 12, an assumed anomalous star, marked in blue) lies much further away from the cluster mean than our other targets. We rejected this star from further analysis as its proper motion differs by 3.3σ from the mean of the other stars. Furthermore, this star is located in the central crowded region of the cluster and therefore has unreliable photometric and spectroscopic data. We ended up with a sample of 11 RGB stars (5 anomalous and 6 normal stars).

The mean proper motion of these stars is:

$$pm_{RA} = 6.69 \pm 0.14 \text{mas/year}$$

$$pm_{DEC} = -2.48 \pm 0.20 \text{mas/year}$$

This is in very good agreement with Vasiliev and Baumgardt (2021), who obtained a mean value for the cluster of $pm_{RA} = 6.69 \pm 0.024$mas/year and $pm_{DEC} = -2.53 \pm 0.024$mas/year. Considering both radial velocity and proper motion analysis, as well as position in the cluster and along the main cluster loci in the CMD, we conclude that our final sample of 11 stars are all bona fide cluster members.

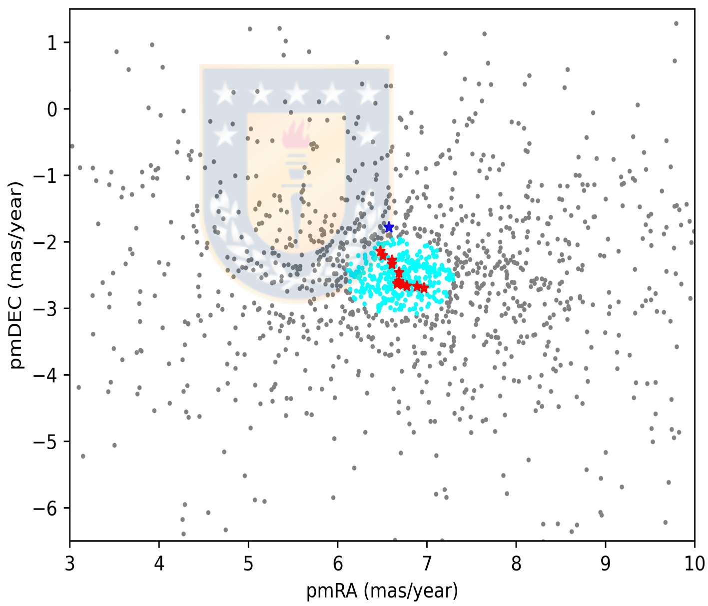

Figure 3.2: Proper motions in the field of NGC 362. Possible cluster members within a 0.6 mas/year circle are indicated with cyan dots, while our targets are represented as red filled stars. The blue filled star represents the rejected star number 12. Data was taken from GAIA eDR3 survey (Collaboration et al., 2020).

Table 3.2 lists the basic parameters of the eleven final members: ID, coordinates, proper motions, G, B_p, R_p magnitudes from GAIA DR2, F275W, F336W, F438W, F606W, F814W magnitudes from HST photometry, and heliocentric radial velocities. The V band was calculated using the F438W, F606W and F814W filters (Harris, 2018).

Table 3.2.1: Coordinates, proper motions, V, GAIA and HST photometry, and radial velocities for the 11 target stars. The V band was calculated using F438W, F606W and F814W filters.

ID	RA (°)	DEC (°)	pmRA (mas/yr)	pmDEC (mas/yr)	V (mag)	G (mag)	B_p (mag)	R_p (mag)	F275W (mag)	F336W (mag)	F438W (mag)	F606W (mag)	F814W (mag)	RV_{helio} (km/s)
11	15.77331529496288	-70.84201303750254	6.505	-2.207	13.62	13.375	13.872	12.497	18.765	16.131	15.020	13.415	12.503	225.91
13	15.83355100868370	-70.83207022949118	6.687	-2.463	14.07	13.841	14.385	13.094	18.591	16.188	15.319	13.883	13.014	230.30
14	15.84985498855671	-70.84020798422353	6.606	-2.279	14.09	13.856	14.363	13.077	18.621	16.144	15.313	13.893	13.012	222.99
15	15.80960339082632	-70.86619177758531	6.685	-2.597	14.35	14.147	14.616	13.398	18.527	16.386	15.610	14.172	13.356	230.55
16	15.75481176194973	-70.83878187983893	6.966	-2.696	14.50	14.300	14.766	13.570	18.389	16.236	15.621	14.324	13.514	226.95
17	15.79282209680344	-70.83773058066414	6.606	-2.335	13.05	12.736	13.402	11.896	19.236	16.225	14.667	12.815	11.798	225.40
18	15.84874591604511	-70.86713946413691	6.478	-2.139	13.19	12.897	13.584	12.096	18.787	16.065	14.697	12.961	11.957	218.33
19	15.86879292727561	-70.85824653897895	6.665	-2.629	13.31	13.018	13.672	12.227	18.862	16.015	14.804	13.085	12.100	215.49
20	15.78729221784991	-70.86387947858030	6.775	-2.665	13.35	13.071	13.686	12.258	18.754	16.028	14.769	13.134	12.173	211.90
21	15.79577687002238	-70.86514268003519	6.886	-2.667	13.44	13.167	13.794	12.378	18.830	15.973	14.847	13.226	12.277	215.72
22	15.82674179749346	-70.86406858433082	6.728	-2.645	14.40	14.205	14.696	13.480	18.169	16.108	15.553	14.223	13.391	217.04

Chapter 4

Atmospheric Parameters Determination

In order to obtain the atmospheric parameters Effective Temperature, Surface Gravity, Microturbulence and Metallicity, we used three different methods:

4.1 First Method: The CMD isochrone-fitting method and EQW

In the first, we derived T_{eff} and log(g) by comparing the F606W vs. (F606W-F814W) CMD from HST photometry and the G vs. (B_P-R_P) CMD from GAIA photometry with isochrones obtained from the PARSEC database (Bressan et al., 2012). The fit is shown in Figure 4.1. We obtained the best fit for an age of 10.5 Gyrs in both cases. The reddenings and distance moduli we estimated are E(F606W-F814W)=0.02 and $(\text{m-M})_{F606W}$=14.85 for the HST CMD, and E(B_P-R_P)=0.05 and $(\text{m-M})_G$=14.85 for the GAIA CMD, which are in good agreement with Harris (2010) who found values of E(B-V)=0.05 and $(\text{m-M})_V$=14.83. The other key parameter to select an isochrone is the metallicity, but PARSEC isochrones use solar-scaled abundances while GCs are α-enhanced. A way to overcome this discrepancy is to use a global metallicity [M/H] that is calculated taking both [Fe/H] and α-enhancement into account and using the equation from Salaris et al. (1993). However [Fe/H] and [α/Fe] are obtained only when atmospheric parameters are known. For this reason, we had to make an initial guess for [Fe/H] and [α/Fe] based on the literature and then make an initial estimation for T_{eff} and log(g). Using these parameters we then obtained revised estimates for [Fe/H] and [α/Fe] and iterated the process until convergence. Our final value for the mean cluster metallicity is [Fe/H]=-1.1 (see Chapter 5) and using [α/Fe]=+0.3 we get [M/H]=-0.9. Another issue we had to solve is the discrepancy between the color of the isochrones and the color of the stars in the upper RGB since Figure 4.1 shows that isochrones tend to be redder than real stars, especially when we consider the G vs. (B_P-R_P) CMD. This is not surprising since isochrones are transformed from the theoretical temperature-luminosity plane to the observational plane by synthetic temperature-color relations. These relations are calculated using synthetic spectra that poorly reproduce the spectra of the very cool upper RGB stars, especially in the blue-UV part. We found that the best way to overcome this problem is projecting horizontally the position of the star in the CMD until it intersects the isochrone and assuming its T_{eff} and log(g) to be the temperature and gravity of the point of the isochrones that have the same F606W or G magnitude. The results of this first method are reported in Table 4.1.1.

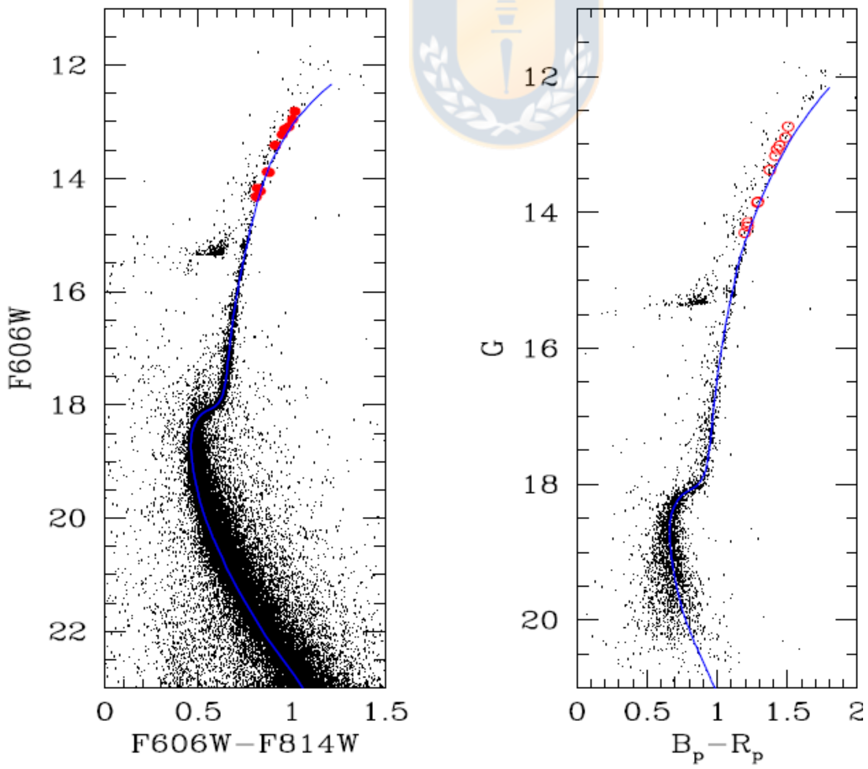

Figure 4.1: CMDs of NGC 362 from HST and GAIA photometry with isochrones obtained from PARSEC database (Bressan et al., 2012). Red symbols represent the observed RGB stars.

We check the gravities by the canonical equation:

$$\log\left(\frac{g}{g_\odot}\right) = \log\left(\frac{M}{M_\odot}\right) + 4\log\left(\frac{T_{\rm eff}}{T_\odot}\right) - \log\left(\frac{L}{L_\odot}\right)$$

where the mass M was assumed to be 0.9 $M_\odot$ from the isochrone fitting, and the luminosity $L/L_\odot$ was obtained from the absolute magnitude M_V assuming an apparent distance modulus of $(m\text{-}M)_V$=14.83 from Harris (1996). The bolometric correction (BC) was derived by adopting the relation BC-$T_{\rm eff}$ from Alonso et al. (1999). Both distance modulus and BC are valid for the Johnson V band, while we have HST magnitudes. For this reason, we transformed F438W, F606W and F814W magnitudes into Johnson B,V and I magnitudes using the transformations from Harris (2018). The V magnitudes and gravities we obtained are reported in Table 3.2.1 and Table 4.1.1 respectively. Table 4.1.1 shows that gravities from isochrones agree very well with those obtained from the canonical equation and also that $T_{\rm eff}$ and log(g) obtained independently from HST and GAIA data match each other within the errors.

For the iron content determination we used the parameters we obtained from the HST data. We also have to determine microturbulence v_t together with [Fe/H]. This determination relies on the abundances obtained from equivalent width (EQW) of FeI lines as measured from the spectra. EQWs were measured fitting a gaussian to unblended and well defined iron lines. The line-list we used is the same used in previous papers (e.g., Villanova et al. 2013), so we refer to those articles for a detailed discussion about this point. We underline here that particular care was applied to the continuum determination. First of all, atmospheric models were calculated using the ATLAS9 code (Kurucz, 1970), assuming our photometric estimations of $T_{\rm eff}$ and log(g) as an initial guess. We assume also v_t=1.5 km/s and [Fe/H]=-1.1 as initial estimations. Then v_t was re-adjusted and new atmospheric models calculated in an interactive way in order to remove trends in reduced equivalent width versus abundance plots. About 100 FeI lines (depending on the S/N of the spectrum) were used for this purpose. The [Fe/H] value of the model was changed at each iteration according to the output of the abundance analysis. The Local Thermodynamic Equilibrium (LTE) program MOOG (Sneden, 1973) was used for the abundance analysis. Final microturbulence and metallicities are reported in Table 4.1.1.

Table 4.1.1: Columns 2-9: T_{eff} and log(g) obtained through isochrone fitting using GAIA and HST data with two different metallicities (-1.1 and -0.9). Column 10: log(g) obtained from the canonical equation. Columns 11-12: T_{eff} and log(g) used to calculate v_t and Fe. Columns 13-14: Microturbulence and metallicities obtained assuming T_{eff} and log(g) from columns 11 and 12, and using FeI lines from the spectra. Column 15: Classification of the stars, 'n' for normal and 'a' for anomalous.

ID	$T_{GAIA_{m11}}$	$g_{GAIA_{m11}}$	$T_{GAIA_{m09}}$	$g_{GAIA_{m09}}$	$T_{HST_{m11}}$	$g_{HST_{m11}}$	$T_{HST_{m09}}$	$g_{HST_{m09}}$	$\log(g)_{phot}$	T_{eff}	log(g)	v_t	[Fe/H]	Class
11	4405	1.28	4306	1.27	4415	1.30	4303	1.26	1.25	4303	1.26	1.61	-1.11	a
13	4558	1.56	4465	1.55	4573	1.58	4470	1.56	1.55	4470	1.56	1.40	-1.02	a
14	4563	1.56	4470	1.56	4576	1.59	4473	1.56	1.56	4473	1.56	1.48	-1.11	a
15	4652	1.73	4563	1.72	4662	1.74	4564	1.73	1.70	4564	1.73	1.44	-1.05	a
16	4696	1.81	4609	1.81	4706	1.83	4610	1.81	1.82	4610	1.81	1.32	-1.07	n
17	4176	0.87	4072	0.85	4187	0.89	4064	0.83	0.88	4064	0.83	1.69	-1.05	a
18	4236	0.98	4132	0.96	4246	1.00	4124	0.94	1.02	4124	0.94	1.51	-1.07	n
19	4281	1.06	4177	1.04	4294	1.08	4175	1.03	1.10	4175	1.03	1.59	-1.18	n
20	4299	1.09	4198	1.07	4312	1.12	4196	1.07	1.14	4196	1.07	1.57	-1.17	n
21	4333	1.15	4232	1.13	4347	1.18	4231	1.13	1.18	4231	1.13	1.54	-1.20	n
22	4669	1.76	4581	1.76	4677	1.77	4580	1.76	1.77	4580	1.76	1.39	-1.07	n

4.2 Second Method: Spectrum Synthesis of the 6137 Å Fe band

Another standard technique to get [Fe/H] from the spectra when T_{eff} and log(g) are known is the spectral synthesis method, which is suitable for low S/N and/or limited wavelength range data. In this case, v_t is obtained from a relation that involves log(g) and also T_{eff} in some cases. We decided to also apply this second method to our spectra as a further check. We used the atmospheric parameters obtained from the HST data and two relations for microturbulence. The first is the empirical relation from Marino, A. F. et al. (2008) that relates log(g) with v_t for RGB stars in GCs, and the other is the theoretical relation from Mott et al. (2020) that was obtained from 3D-NLTE models and that relates log(g) and T_{eff} with v_t. As the Fe indicator, we used a strong Fe band at 6137 Å that is a blend of many FeI lines and that is visible even in low S/N spectra (see Figure 1.10). Again, atmospheric models were calculated using the ATLAS9 code (Kurucz, 1970) and the LTE program MOOG (Sneden, 1973) was used for the abundance analysis. The results are reported in Table 4.2.1.

Table 4.2.1: Columns 2-3: T_{eff} and log(g) from the previous table. Columns 4-5: Microturbulence obtained from the Mott et al. (2020) relation, and metallicity obtained using spectral synthesis of FeI lines and considering vt_{Mott}. Column 6: Microturbulence obtained from the Marino, A. F. et al. (2008) relation. Column 7: Classification of the stars.

ID	T_{eff}	log(g)	vt_{Mott}	[Fe/H]	vt_{Marino}	Class
11	4303	1.26	1.61	-1.09	1.61	a
13	4470	1.56	1.55	-1.05	1.53	a
14	4473	1.56	1.56	-1.09	1.53	a
15	4564	1.73	1.52	-1.04	1.49	a
16	4610	1.81	1.51	-1.06	1.47	n
17	4064	0.83	1.70	-1.09	1.72	a
18	4124	0.94	1.66	-1.10	1.69	n
19	4175	1.03	1.66	-1.13	1.67	n
20	4196	1.07	1.65	-1.10	1.66	n
21	4231	1.13	1.64	-1.13	1.64	n
22	4580	1.76	1.51	-1.10	1.48	n

4.3 Third Method: Atmospheric parameters from spectra and EQW technique

The third method we used to estimate T_{eff} and log(g) relies on the abundances obtained from EQW of FeI and FeII lines as measured from the spectra. Microturbulence and [Fe/H] were also determined in the process. First of all, atmospheric models were calculated again using the ATLAS9 code (Kurucz, 1970), assuming our photometric estimations of T_{eff} and log(g) as initial guesses. We assume also v_t=1.5 km/s and [Fe/H]=-1.1 as initial estimations. Then T_{eff}, log(g), and v_t were re-adjusted and new atmospheric models calculated in an interactive way in order to remove trends in excitation potential and reduced EQW versus abundance in order to derive T_{eff} and v_t, respectively, and to satisfy the ionization equilibrium for log(g). About 100 FeI lines (depending on the S/N of the spectrum) and 4 FeII lines were used for the latter purpose. The [Fe/H] value of the model was changed at each iteration according to the output of the abundance analysis. The LTE program MOOG (Sneden, 1973) was used for this abundance analysis as in the previous methods. Results of this third method are reported in Table 4.3.1.

Table 4.3.1: Parameters and metallicities obtained spectroscopically using the FeI and FeII lines.

ID	T_{eff}	log(g)	v_t	[Fe/H]	Class
11	4297	1.00	1.60	-1.15	a
13	4475	1.58	1.49	-1.04	a
14	4479	1.48	1.49	-1.11	a
15	4486	1.54	1.38	-1.11	a
16	4637	1.69	1.35	-1.05	n
17	4111	0.62	1.70	-1.09	a
18	4209	0.79	1.54	-1.07	n
19	4250	0.90	1.61	-1.16	n
20	4292	1.04	1.58	-1.12	n
21	4300	1.08	1.56	-1.17	n
22	4614	1.74	1.42	-1.05	n

4.4 Comparison of the different techniques

We first compare the atmospheric parameters we obtained using the different techniques explained in the previous section. This is useful to know and quantify possible discrepancies that might exist between the different methods, and to choose the most appropriate depending on the kind of data one is analyzing. We start by comparing T_{eff} and log(g). For this purpose, in the upper panels of Figure 4.2 we report log(g) vs. V magnitude (left panel) and T_{eff} vs. V magnitude (right panel) for our targets. V magnitude has an error that is negligible in the scale of the figure, and any discrepancy visible between the points is due only to discrepancies in gravity and temperature respectively. In the upper panels, red points represent gravities and temperatures obtained using the isochrone-fitting method, green crosses are the same parameters obtained using the FeI and FeII equilibrium, while the black squares on the upper left panel represent log(g) obtained from the canonical equation. The green line is the linear fit to the green crosses. We see that the best agreement between CMD fitting and FeI/II balance happens for the fainter and hotter targets. For bright stars, the FeI/II lines balance method gives gravities and temperatures that are slightly lower and higher (respectively) compared with the CMD fitting method. The discrepancy is of order -0.1 dex in log(g) and +40 K in T_{eff}. On the other hand, the gravity obtained from the canonical equation agrees very well with those obtained by isochrone fitting.

For microturbulence, the lower left panel shows v_t as obtained from EQW of FeI lines and assuming the isochrone method parameters (red points), from the empirical Marino, A. F. et al. (2008) relation (yellow points), from the theoretical Mott et al. (2020) relation (magenta points), and from EQW of FeI lines and assuming the FeI/II lines balance method parameters (green crosses). We underline the very good agreement between the empirical and the theoretical relation in spite of the fact that they were obtained in two completely different ways. Since the relation from Mott et al. (2020) depends also on the temperature, this means that it can be safely used to obtained the microturbulence in evolutionary stages different from the RGB (i.e. AGB, RC, SGB, MS), where the relation from Marino, A. F. et al. (2008) is not valid. On the other hand, v_t obtained from EQW of FeI and parameters from the isochrone-fitting method agrees well with that obtained from EQW of FeI and parameters from the FeI/II lines balance, but are slightly lower (about -0.1 km/s) than that obtained from the Mott et al. (2020) relation.

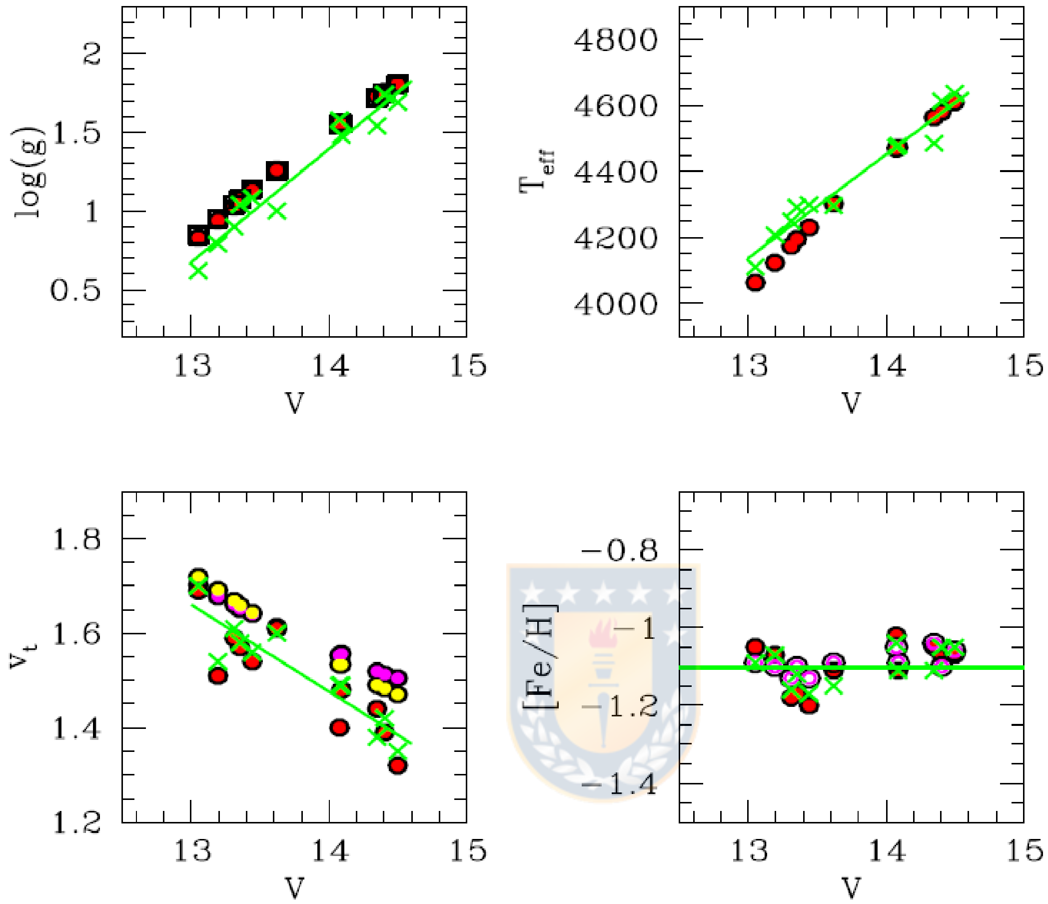

Figure 4.2: Comparison of the estimated atmospheric parameters as a function of V magnitude. The upper panels show log(g) and T_{eff} obtained from the isochrone-fitting method (red points), from the FeI/FeII equilibrium (green crosses), and log(g) from the canonical equation (black squares). In the lower left panel red points represent v_t obtained from EQW of FeI lines and assuming the isochrone-fitting method parameters, while yellow and magenta points represent microturbulences obtained from the Marino, A. F. et al. (2008) and Mott et al. (2020) relations, respectively. Green crosses show v_t as obtained from EQW of FeI lines and assuming the FeI/FeII equilibrium. In the lower right panel red points represent metallicities obtained using T_{eff} and log(g) from the isochrone method and v_t and Fe from the EQW of FeI lines. Magenta points represent [Fe/H] obtained using T_{eff} and log(g) from the isochrone method and v_t and Fe from the Mott et al. (2020) relation and spectral synthesis method, respectively. Green points represent metallicities obtained using atmospheric parameters from the FeI/FeII balance, and Fe from EQW of FeI lines. The green line is the linear fit to the green crosses.

The lower right panel shows finally the impact of the different methods used to obtain the parameters and to estimate the abundance from iron lines on the final [Fe/H] measurement. Here red points represent the metallicities obtained using T_{eff} and log(g) from the isochrone method and microturbulence and metallicity from the EQW of FeI lines. Magenta points represent the metallicities obtained using T_{eff} and log(g) from the isochrone method but the microturbulence from the Mott et al. (2020) relation and the metallicity from the fit of the 6137 Å iron band. Green points represent the metallicities obtained using T_{eff}, log(g), and v_t from the FeI/II lines balance, and the metallicity from the EQW of FeI lines. We see that, in spite of the fact that the three methods used to get the final [Fe/H] values are partially independent from each other, the metallicities agree very well and the systematic difference is very low. The first and third methods give $[Fe/H]_1$=-1.10±0.02 and $[Fe/H]_3$=-1.10±0.01 respectively, while the second returns $[Fe/H]_2$=-1.09±0.01. The only real difference is in the dispersion. The second method returns the lowest spread, with $\sigma_{[Fe/H]_2} = 0.03 \pm 0.01$, while the first and third give $\sigma_{[Fe/H]_1} = 0.06 \pm 0.01$ and $\sigma_{[Fe/H]_3} = 0.05 \pm 0.01$ respectively.

Our conclusion is that, in spite of the fact that the atmospheric parameters obtained from the different methods of analysis we applied show a certain degree of disagreement (however below 50 K in temperature, 0.1 dex in gravity and 0.1 km/s in microturbulence), the final [Fe/H] appears not to be affected by any systematics, at least differentially. We underline also the fact that the quickest method we applied, i.e. T_{eff} and log(g) from the isochrone-fitting method, microturbulence from the Mott et al. (2020) relation and the metallicity from the fit of the 6137 Å iron band, is also the one that returns the data with the lowest spread.

Chapter 5

Results

The mean iron content values we obtained with the three methods are:

$$[Fe/H]_1 = -1.10 \pm 0.02$$

$$[Fe/H]_2 = -1.09 \pm 0.01$$

$$[Fe/H]_3 = -1.10 \pm 0.01$$

with a dispersion of:

$$\sigma_{[Fe/H]_1} = 0.06 \pm 0.01$$

$$\sigma_{[Fe/H]_2} = 0.03 \pm 0.01$$

$$\sigma_{[Fe/H]_3} = 0.05 \pm 0.01$$

The typical internal error on temperature determination is between 20 and 40 K, depending on the method, while the errors on gravity and microturbulence are below 0.1 dex and 0.05 km/s respectively. If we apply the same procedure described in Villanova et al. (2013) and Marino, A. F. et al. (2008) for the error calculation we obtain $\sigma_{\mathrm{TOT}} = 0.05$ for our estimate of the total internal error in metallicity. Comparing this value with the observed spreads, we see that there is no room for an intrinsic metallicity variation in NGC 362. Even more, the second method delivers an iron spread that is 1.7 - 2 times lower that the other two, strengthening our statement.

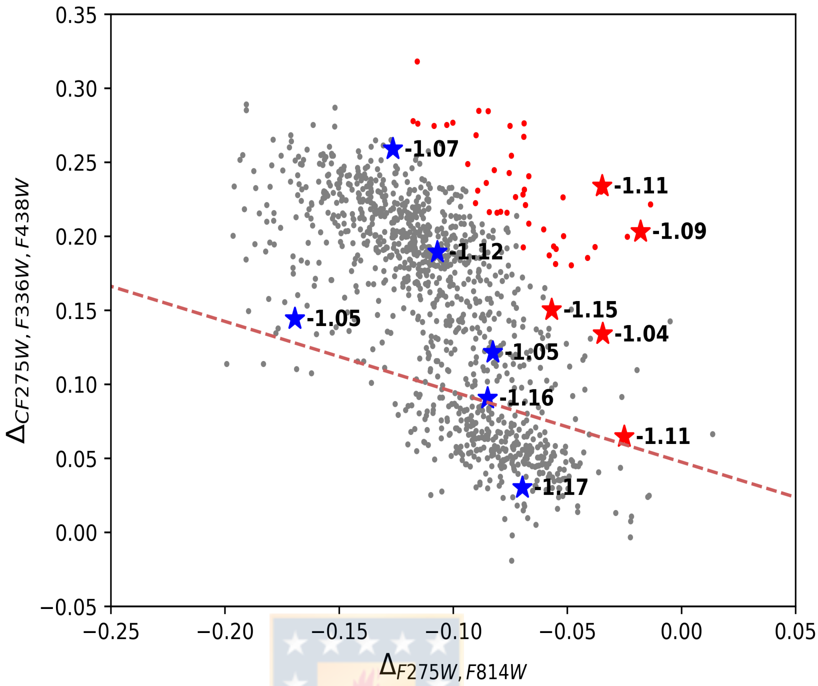

Figure 5.1: Chromosome map of NGC 362 with each target's spectroscopically-derived metallicity noted.

Figure 5.1 shows the chromosome map of NGC 362 with the typical separation between 1G (lower) and 2G (upper) stars divided by the magenta dashed line. The significant distribution of red (anomalous) stars located on the right part of the main loci of 1G and 2G (normal) stars is the cause for the classification of NGC 362 as Type II (Milone et al., 2017). According to their scenario, the anomalous stars should have an iron content higher than the normal population. As we mentioned earlier, our target stars were chosen to cover a wide range in the chromosome map in order to allow us to check if an iron spread is indeed present. We carefully selected an equal number of normal and anomalous stars in order to best test the possibility of a predicted metallicity variation between them. In the end, we obtained very good spectra for 6 normal and 5 anomalous members of NGC 362.

In spite of the classification of NGC 362 as a Type II cluster, the measured iron dispersion does not support the existence of a significant iron spread in our sample. In our sample we have 5 anomalous stars, located on the red side of the main 1G and 2G populations and for this reason, according to Milone et al. (2017), they should show a [Fe/H] value significantly larger (0.1-0.2 dex) than the normal stars.

However, their spectroscopically-derived [Fe/H] content spans the range -1.04 to -1.15 dex, insignificantly different from the spread of the 6 normal stars (-1.05 to -1.17 dex). What's more, looking in detail at the spectroscopic results of our target stars in each group, we find a mean metallicity of $[Fe/H]_n$=-1.10±0.02 with a spread of σ_n=0.04±0.01 for the 6 normal stars vs. $[Fe/H]_a$=-1.10±0.02 with a spread of σ_a=0.05±0.01 for the 5 anomalous stars. This confirms our main result: that NGC 362 does not host stars with an intrinsic iron spread, and in particular there is no metallicity difference between normal and anomalous stars.

5.1 Comparing our results with the literature

We now discuss how our result compares to results in the literature. It is worth noting that our study is the first one that purposefully compares metallicities in normal vs. anomalous stars in NGC 362. Worley and Cottrell (2010) analyzed the high-resolution spectra of 13 giant stars in NGC 362 taken with the UVES spectrograph. Fe, light (Sr, Y, Zr) and heavy (Ba, Nd, La) s-process element abundances were derived from EQWs. They found an average metallicity of [Fe/H]=-1.21±0.09 and light and heavy abundances of [ls/Fe]=0.32±0.10 dex and [hs/Fe]=0.46±0.09 dex, respectively. The small spread in these values and the lack of trend of [hs/ls] with metallicity, indicates a clear homogeneity in the s-process elemental abundance enhancements for NGC 362. It also indicates that the spread in the overall derived metallicity for these stars is due to the analysis rather than intrinsic differences between the stars.

Carretta et al. (2013) obtained FLAMES GIRAFFE+UVES high-resolution spectra for both first and second generation stars in NGC 362 and used them to derive abundances of proton-capture, α-capture, Fe-peak and neutron-capture elements from EQWs. The mean metallicity found with UVES and GIRAFFE spectra was [Fe/H]=-1.17±0.05 dex (for a sample of 14 stars) and [Fe/H]=-1.17±0.06 dex (for 90 targets) respectively. The authors did not find evidence for an internal metallicity spread. Nevertheless they discovered the presence of an additional, poorly populated (e.g., accounting for only ∼6 per cent of the total cluster population) red RGB sequence which appears to be enriched in s-process elements, particularly in Ba.

Bailin (2019) presented an up-to-date catalog of intrinsic iron abundance spreads in 55 Milky Way GCs for which sufficiently precise spectroscopic measurements were available. Bailin homogeneously reanalyzed the spectroscopic data from Worley and Cottrell (2010) for NGC 362 and measured an average metallicity of [Fe/H]=-1.21±0.02 with a dispersion of σ=0.07. He did not find any trace of an intrinsic iron spread. He also reported a trend of larger metallicity dispersion with higher luminosity for GCs with $L > 10^5 L_\odot$.

Mészáros et al. (2020) investigated the Fe, C, N, O, Mg, Al, Si, K, Ca, Ce and Nd abundances in 31 GCs from high-resolution spectra observed by the SDSS-IV APOGEE-2 survey. They collected spectra for 56 RGB stars in NGC 362 and used the BACCHUS code (Masseron et al., 2016) to determine metallicities and abundances. The mean iron content obtained was [Fe/H]=-1.03±0.06 with a dispersion of σ=0.08. Mészáros et al. found no indication for an internal metallicity variation, however they have not investigated if any Fe spread exists between normal and anomalous stars. When looking at other elements, the authors found clear Al-O anticorrelation and Al-N correlation with a weakly present Al-Mg anticorrelation, in addition to a small Al spread of $[Al/Fe]_{scatter}$=0.24. On the other hand, a uniform and constant C+N+O content was measured. Finally a clear s-process element enhancement was reported, confirming the study of Carretta et al. (2013). A future paper will report on abundances of a large number of species, including s-process elements.

Thus, there is an array of existing studies of the metallicities of a significant number of stars based on high-resolution spectroscopy. Although our's is the first to explicitly select purported normal and anomalous stars a priori, other studies undoubtedly included both types of stars in their large samples, especially the studies of Carretta et al. (2013) and Mészáros et al. (2020). The concatenation of this observational evidence does not support the hypothesis of Milone et al. (2017) that NGC 362 is characterised by an intrinsic iron spread, with our study being the most decisive, at least in terms of preselecting normal and anomalous stars. It is extremely unlikely that a real spread was simply missed due to improper and/or small samples or large errors.

Lardo et al. (2016) reported that spurious spreads observed in the s-process rich group of stars are derived in anomalous GCs (i.e. clusters with spreads in s-process elements and possibly C+N+O, double SGBs and split RGBs) when spectroscopic gravities are adopted. Such clusters would be indeed mono-metallic when FeII lines and photometric gravities were used in the analysis. Carretta et al. (2013) adopted photometric stellar gravities and they did not report an [Fe/H] spread for stars in NGC 362, which is consistent with the hypothesis that spectroscopic gravities might yield artificial iron spreads. However, note that Muñoz et al. (2021) find an intrinsic spread in the Type II GC NGC 1261, using both photometric and spectroscopic gravities.

5.2 Other Type II GCs with presumed Fe spreads

Given the importance of understanding Type II GCs formation and evolution, it is of great interest to investigate with high-resolution spectra other Type II GCs with presumed metallicity spreads. Of the ten Type II GCs identified by Milone et al. (2017), Mészáros et al. (2020) derived abundances and discussed intrinsic iron spreads for NGC 362, NGC 1851, ω Centauri, NGC 6388, M22 and NGC 7089, while Bailin (2019) studied NGC 5289 and NGC 6715. Marino et al. (2018) analyzed the lowest mass Type II GC NGC 6934 and more recently Muñoz et al. (2021) performed a detailed metallicity analysis of the second lowest mass GC NGC 1261. From the existing data it is not clear that all of these GCs presumed to have Fe spreads may in fact possess them. Mészáros et al. (2020) do not confirm the large metallicity spread previously observed in NGC 1851 and Carretta et al. (2010) find no variation in the [Fe/H] abundances of NGC 362, NGC 6388, M22 and NGC 7089. The only real spreads found were in ω Centauri and NGC 6715. However, both of these objects are classified as the remnant cores of tidally disrupted (or disrupting) dwarf galaxies and hence have a different chemical evolution history from typical GCs. Bailin (2019) confirmed a metallicity spread in NGC 6715 as well as in the Type II GC NGC 5286. Moreover, he reported that the former has the second largest Fe spread of his study, with the largest belonging to ω Centauri. Regarding the two lowest mass Type II GCs, NGC 1261 and NGC 6934, they do both show evidence for an intrinsic metallicity variation, although both studies used a small sample of stars.

5.2.1 The highly debated iron spread in M22

The existence of an intrinsic real Fe spread in M22 has been highly debated in the literature since spectroscopic and photometric studies based on small samples of stars have yielded conflicting results. Cohen (1981) and Gratton (1982) conclude that no significant metallicity variation is present in this Type II GC, while Pilachowski et al. (1982) and Lehnert et al. (1991) found evidence of an intrinsic Fe spread, with -1.4<[Fe/H]<-1.9. Marino et al. (2009) confirmed the existence of an intrinsic Fe variation from the analysis of high-resolution UVES spectra of 17 stars, reporting that the difference between the mean Fe abundances of the two identified groups of stars is 0.14 dex. More recently, Marino et al. (2011b) analyzed high-resolution spectra of 35 giant stars, finding that M22 hosts at least two groups of stars characterized by substantial star-to-star metallicity scatter (-2.0$\lesssim$[Fe/H]$\gtrsim$-1.6), s-process and CNO-cycle elements. Thus, this cluster was able to retain the typical high-mass AGB ejecta, as well as the SNe ejecta. Mucciarelli et al. (2015) presented a new high-resolution spectra analysis of 17 giant stars that Marino et al. (2009) used to provide evidence in support to an intrinsic metallicity spread in M22, and found that when surface gravities are derived spectroscopically the [Fe/H] distribution spans $\sim$0.5 dex, but when photometric gravities are adopted, the [FeII/H] distribution shows no evidence of an iron spread, concluding that M22 is a normal GC and ruling out that it has retained the supernovae ejecta in its gravitational potential well. The later spectroscopic study of Mészáros et al. (2020) do not observe a significant Fe variation in M22 either, reporting a [Fe/H]=-1.52$\pm$0.02 with a dispersion of σ=0.11, expected from the internal errors, based on a sample of 20 high S/N spectra observed with APOGEE.

The analysis of Muñoz et al. (2021) does not find any relation between intrinsic metallicity spread and either GC mass, the fraction of Type II stars (N_{TypeII}/N_{Tot}) or the fraction of 1G stars (N_1/N_{Tot}). In particular, NGC 362 does not stand out in any of these plots. Its mass is greater than that of either of the two very low mass Type II GCs, NGC 1261 and NGC 6934, both of which appear to have real spreads, comparable to that of intermediate mass Type IIs that do not appear to have spreads, and of course much less than the masses of NGC 6715 and ω Centauri.

Figure 5.2: The Globular Cluster M22 observed by the Hubble Space Telescope. Image Credits: ESA/Hubble & NASA.

Chapter 6

Conclusions and Future Prospects

6.1 Summary and Conclusions

In this paper we have presented a chemical characterization of the GC NGC 362, which is classified as a Type II GC by Milone et al. (2017), focusing on the metallicity. Marino et al. (2018) suggests that Type II GCs possess an intrinsic variation in metallicity, with anomalous stars (those lying both on the reddest RGB as well as to the red of the chromosome map) predicted to have higher metallicity than normal main RGB or chromosome map stars. We observed twelve RGB stars using the high-resolution MIKE spectrograph mounted at the Magellan-Clay telescope. The stars were carefully selected from HST UV Legacy data to include a comparable sample of normal and anomalous stars. One of the anomalous stars proved to be a less-likely proper motion member, as well as overly spatially crowded, and was discarded. From the spectra and HST and GAIA photometry, we determined the atmospheric parameters and measured the iron content of all of our sample with three different methods, and then derived the mean metallicity and its dispersion for each method:

- First method: The iron content was obtained using $T_{\rm eff}$ and log(g) from the isochrone-fitting method, and v_t and metallicity from the EQW of FeI lines. This method returns $[Fe/H]_1 = -1.10 \pm 0.02$ and $\sigma_{[Fe/H]_1} = 0.06 \pm 0.01$.
- Second method: [Fe/H] was determined using $T_{\rm eff}$ and log(g) from the CMD isochrones fitting method and v_t from the Mott et al. (2020) relation. We used spectral synthesis to obtain the metallicity from the fit of the 6137 Å iron band.

This method returns $[Fe/H]_2 = -1.09 \pm 0.01$ and $\sigma_{[Fe/H]_2} = 0.03 \pm 0.01$.

- Third method: The iron abundance was obtained using T_{eff}, log(g) and v_t from the FeI and FeII lines balance, and the metallicity from the EQW of FeI lines. This method returns $[Fe/H]_3 = -1.10 \pm 0.01$ and $\sigma_{[Fe/H]_3} = 0.05 \pm 0.01$.
- The error analysis gives an internal error of 0.05 dex. Comparing these values, we conclude that NGC 362 does not show any trace of an internal iron spread.
- The three methods we used return the same mean iron abundance within the errors, in spite of the fact that they are partially independent from each other. In particular, we find no significant difference between the metallicity of the normal vs. anomalous stars, therefore we do not confirm the hypothesis of Milone et al. (2017). Additionally, previous high-resolution spectroscopic studies of large samples of stars in NGC 362 in the literature did not report any evidence for an intrinsic metallicity variation, endorsing our results.
- We predict that the anomalous stars have an enhanced s-process abundance compared to normal stars, which would explain the Type II behaviour of this cluster.
- The recent paper by Muñoz et al. (2021) does not find any significant relation between intrinsic metallicity spread and either GC mass, (N_{TypeII}/N_{Tot}) or (N_1/N_{Tot}) in Type II GCs. Indeed, they suggest that a number of well studied Type II GCs in fact do not possess intrinsic Fe abundance spreads, and therefore the scenario of Milone et al. (2017) is not fully borne out. Although several GCs with classically-known metallicity spreads, viz. ω Centauri and NGC 6715, are also Type II GCs, and several low mass Type II GCs also appear to have intrinsic metallicity spreads (NGC 1261 and NGC 6934), the other Type II GCs do not clearly demonstrate this phenomenon.

6.2 Future Work

As mentioned in previous chapters, anomalous stars belonging to the faint SGB and red RGB of well-studied Type II GCs are enhanced in Fe, global C+N+O content, and generally, in s-process elements, meaning they possess a metallicity spread. For this reason, we will investigate our prediction that the anomalous stars are enhanced in s-process elements in a future paper. In addition, we will derive the abundances of a large number of species, including: Mg, Si, Ca, Ti, Cr, Fe, and Ni, abundance measurements using the EQWs method; and O, Na, Al, Sc, V, Mn, Co, Cu, Zn, Y, Zr, Ba, La, Ce, Pr, Nd, Sm, Eu, Dy and Pb, using the spectrum-synthesis method.

Bibliography

Alonso, A., Arribas, S., and Martínez-Roger, C. (1999). The effective temperature scale of giant stars (F0-K5). II. Empirical calibration of T_{eff} versus colours and [Fe/H]. *The Astronomical Journal*, 140:261–277.

Arnould, M., Goriely, S., and Jorissen, A. (1999). Non-explosive hydrogen and helium burnings: abundance predictions from the NACRE reaction rate compilation. *Astronomy & Astrophysics*, 347:572–582.

Bailin, J. (2019). Globular cluster intrinsic iron abundance spreads. i. catalog. *The Astrophysical Journal Supplement Series*, 245(1):5.

Baumgardt, H. and Hilker, M. (2018). A catalogue of masses, structural parameters, and velocity dispersion profiles of 112 milky way globular clusters. *Monthly Notices of the Royal Astronomical Society*, 478(2):1520–1557.

Baumgardt, H., Hilker, M., Sollima, A., and Bellini, A. (2019). Mean proper motions, space orbits, and velocity dispersion profiles of Galactic globular clusters derived from Gaia DR2 data. *Monthly Notices of the Royal Astronomical Society*, 482(4):5138–5155.

Becker, S. A. and Iben, I., J. (1979). The asymptotic giant branch evolution of intermediate-mass stars as a function of mass and composition. I. Through the second dredge-up phase. *The Astrophysical Journal*, 232:831–853.

Bedin, L. R., Piotto, G., Anderson, J., Cassisi, S., King, I. R., Momany, Y., and Carraro, G. (2004). ω Centauri: The Population Puzzle Goes Deeper. *The Astrophysical Journal, Letters*, 605(2):L125–L128.

Bekki, K. and Norris, J. E. (2006). The Origin of the Double Main Sequence in ω Centauri: Helium Enrichment due to Gas Fueling from Its Ancient Host Galaxy? *The Astrophysical Journal, Letters*, 637(2):L109–L112.

Bernstein, R., Shectman, S., Gunnels, S., Mochnacki, S., and Atheya, A. (2003). Mike: A double echelle spectrograph for the magellan telescopes at las campanas observatory. *Proceedings of SPIE - The International Society for Optical Engineering*, 4841.

Bressan, A., Marigo, P., Girardi, L., Salasnich, B., Dal Cero, C., Rubele, S., and Nanni, A. (2012). parsec: stellar tracks and isochrones with the padova and trieste stellar evolution code. *Monthly Notices of the Royal Astronomical Society*, 427(1):127–145.

Carretta, Bragaglia, A., Gratton, R. G., Lucatello, S., Catanzaro, G., Leone, F., Bellazzini, M., Claudi, R., D'Orazi, V., Momany, Y., Ortolani, S., Pancino, E., Piotto, G., Recio-Blanco, A., and Sabbi, E. (2009). Na-o anticorrelation and hb - vii. the chemical composition of first and second-generation stars in 15 globular clusters from giraffe spectra. *A&A*, 505(1):117–138.

Carretta, Bragaglia, A., Gratton, R. G., Lucatello, S., D´Orazi, V., Bellazzini, M., Catanzaro, G., Leone, F., Momany, Y., and Sollima, A. (2013). Ngc 362: another globular cluster with a split red giant branch. *A&A*, 557:A138.

Carretta, E., Gratton, R. G., Lucatello, S., Bragaglia, A., Catanzaro, G., Leone, F., Momany, Y., D'Orazi, V., Cassisi, S., D'Antona, F., and et al. (2010). Abundances for a large sample of red giants in ngc 1851: Hints for a merger of two clusters? *The Astrophysical Journal*, 722(1):L1–L6.

Cohen, J. G. (1981). Abundances in globular cluster red giants. IV. M 22 and omega Centauri. *The Astrophysical Journal*, 247:869–878.

Collaboration, G., Brown, A. G. A., Vallenari, A., Prusti, T., de Bruijne, J. H. J., Babusiaux, C., and Biermann, M. (2020). Gaia early data release 3: Summary of the contents and survey properties.

D'Antona, Caloi, V., Montalbán, J., Ventura, P., and Gratton, R. (2002). Helium variation due to self-pollution among globular cluster stars - consequences on the horizontal branch morphology. *A&A*, 395(1):69–75.

de Mink, S. E., Pols, O. R., Langer, N., and Izzard, R. G. (2009). Massive binaries as the source of abundance anomalies in globular clusters. *Astronomy & Astrophysics*, 507(1):L1–L4.

Decressin, T., Charbonnel, C., and Meynet, G. (2007). Origin of the abundance patterns in Galactic globular clusters: constraints on dynamical and chemical properties of globular clusters. *Astronomy & Astrophysics*, 475(3):859–873.

Decressin, T., Meynet, G., Charbonnel, C., Prantzos, N., and Ekström, S. (2007). Fast rotating massive stars and the origin of the abundance patterns in galactic globular clusters. *Astronomy & Astrophysics*, 464(3):1029–1044.

D'Ercole, A., Vesperini, E., D'Antona, F., McMillan, S. L. W., and Recchi, S. (2008). Formation and dynamical evolution of multiple stellar generations in globular clusters. *Monthly Notices of the Royal Astronomical Society*, 391(2):825–843.

D'Ercole, A., Vesperini, E., D'Antona, F., McMillan, S. L. W., and Recchi, S. (2008). Formation and dynamical evolution of multiple stellar generations in globular clusters. *Monthly Notices of the Royal Astronomical Society*, 391(2):825–843.

Dwek, E. (2016). Iron: A key element for understanding the origin and evolution of interstellar dust. *The Astrophysical Journal*, 825(2):136.

Ferraro, F. R., Dalessandro, E., Mucciarelli, A., Beccari, G., Rich, R. M., Origlia, L., Lanzoni, B., Rood, R. T., Valenti, E., Bellazzini, M., and et al. (2009). The cluster terzan 5 as a remnant of a primordial building block of the galactic bulge. *Nature*, 462(7272):483–486.

Gratton, R. G. (1982). Abundances in metal-poor stars. I. The globular clusters NGC 2808, NGC 3201, NGC 6397, and M 22. *Astronomy & Astrophysics*, 115:171–184.

Harris, W. E. (1996). A catalog of parameters for globular clusters in the milky way. *The Astronomical Journal*, 112:1487.

Harris, W. E. (2010). A new catalog of globular clusters in the milky way.

Harris, W. E. (2018). Transformation of hst wfc3/uvis filters to the standard bvi system. *The Astronomical Journal*, 156:296.

Kelson, D., Illingworth, G., Dokkum, P. V., and Franx, M. (2000). The evolution of early-type galaxies in distant clusters. iii. m/l-v ratios in the z=0.33 cluster cl 1358+62. *The Astrophysical Journal*, 531:184–199.

Kelson, D. D. (2003). Optimal techniques in two-dimensional spectroscopy: Background subtraction for the 21st century. *Publications of the Astronomical Society of the Pacific*, 115(808):688–699.

Kharchenko, Piskunov, A. E., Schilbach, E., Röser, S., and Scholz, R.-D. (2013). Global survey of star clusters in the milky way - ii. the catalogue of basic parameters. *A&A*, 558:A53.

Kroupa, P. (2001). On the variation of the initial mass function. *Monthly Notices of the Royal Astronomical Society*, 322(2):231–246.

Kurucz, R. L. (1970). Atlas: a Computer Program for Calculating Model Stellar Atmospheres. *SAO Special Report*, 309.

Lardo, C., Mucciarelli, A., and Bastian, N. (2016). The iron dispersion of the globular cluster m2, revised. *Monthly Notices of the Royal Astronomical Society*, 457(1):51–63.

Lehnert, M. D., Bell, R. A., and Cohen, J. G. (1991). Abundances in the red giants of m13 and m22. *Astrophysical Journal; (USA)*, 367.

Majewski, S. R., Patterson, R. J., Dinescu, D. I., Johnson, W. Y., Ostheimer, J. C., Kunkel, W. E., and Palma, C. (2000). ω Centauri : Nucleus of a milky way dwarf spheroidal ? In Noels, A., Magain, P., Caro, D., Jehin, E., Parmentier, G., and Thoul, A. A., editors, *Liege International Astrophysical Colloquia*, volume 35 of *Liege International Astrophysical Colloquia*, page 619.

Marino, Sneden, C., Kraft, R. P., Wallerstein, G., Norris, J. E., Da Costa, G., Milone, A. P., Ivans, I. I., Gonzalez, G., Fulbright, J. P., Hilker, M., Piotto, G., Zoccali, M., and Stetson, P. B. (2011a). The two metallicity groups of the globular cluster m a chemical perspective. *A&A*, 532:A8.

Marino, Sneden, C., Kraft, R. P., Wallerstein, G., Norris, J. E., Da Costa, G., Milone, A. P., Ivans, I. I., Gonzalez, G., Fulbright, J. P., Hilker, M., Piotto, G., Zoccali, M., and Stetson, P. B. (2011b). The two metallicity groups of the globular cluster m a chemical perspective. *A&A*, 532:A8.

Marino, A. F., Milone, A. P., Piotto, G., Villanova, S., Bedin, L. R., Bellini, A., and Renzini, A. (2009). A double stellar generation in the globular cluster NGC 6656 (M 22). Two stellar groups with different iron and s-process element abundances. *Astronomy & Astrophysics*, 505(3):1099–1113.

Marino, A. F., Yong, D., Milone, A. P., Piotto, G., Lundquist, M., Bedin, L. R., Chené, A.-N., Costa, G. D., Asplund, M., and Jerjen, H. (2018). Metallicity variations in the type ii globular cluster ngc 6934. *The Astrophysical Journal*, 859(2):81.

Marino, A. F., Villanova, S., Piotto, G., Milone, A. P., Momany, Y., Bedin, L. R., and Medling, A. M. (2008). Spectroscopic and photometric evidence of two stellar populations in the galactic globular cluster ngc 6121 (m***. *A&A*, 490(2):625–640.

Masseron, T., Merle, T., and Hawkins, K. (2016). BACCHUS: Brussels Automatic Code for Characterizing High accUracy Spectra.

Milone, A. P., Piotto, G., Renzini, A., Marino, A. F., Bedin, L. R., Vesperini, E., D'Antona, F., Nardiello, D., Anderson, J., King, I. R., Yong, D., Bellini, A., Aparicio, A., Barbuy, B., Brown, T. M., Cassisi, S., Ortolani, S., Salaris, M., Sarajedini, A., and van der Marel, R. P. (2017). The Hubble Space Telescope UV Legacy Survey of Galactic globular clusters – IX. The Atlas of multiple stellar populations. *Monthly Notices of the Royal Astronomical Society*, 464(3):3636–3656.

Minniti, D., Lucas, P. W., Emerson, J. P., Saito, R. K., Hempel, M., Pietrukowicz, P., Ahumada, A. V., Alonso, M. V., Alonso-Garcia, J., Arias, J. I., Bandyopadhyay, R. M., Barbá, R. H., Barbuy, B., Bedin, L. R., Bica, E., Borissova, J., Bronfman, L., Carraro, G., Catelan, M., Clariá, J. J., Cross, N., de Grijs, R., Dékány, I., Drew, J. E., Fariña, C., Feinstein, C., Fernández Lajús, E., Gamen, R. C., Geisler, D., Gieren, W., Goldman, B., Gonzalez, O. A., Gunthardt, G., Gurovich, S., Hambly, N. C., Irwin, M. J., Ivanov, V. D., Jordán, A., Kerins, E., Kinemuchi, K., Kurtev, R., López-Corredoira, M., Maccarone, T., Masetti, N., Merlo, D., Messineo, M., Mirabel, I. F., Monaco, L., Morelli, L., Padilla, N., Palma, T., Parisi, M. C., Pignata, G., Rejkuba, M., Roman-Lopes, A., Sale, S. E., Schreiber, M. R., Schröder, A. C., Smith, M., , L. Sodré, J., Soto, M., Tamura, M., Tappert, C., Thompson, M. A., Toledo, I., Zoccali, M., and Pietrzynski, G. (2010). VISTA Variables in the Via Lactea (VVV): The public ESO near-IR variability survey of the Milky Way. 15(5):433–443.

Mott, Steffen, M., Caffau, E., and Strassmeier, K. G. (2020). Improving spectroscopic lithium abundances - fitting functions for 3d non-lte corrections in fgk stars of different metallicity. *A&A*, 638:A58.

Muñoz, C., Geisler, D., Villanova, S., Sarajedini, A., Frelijj, H., Vargas, C., Monaco, L., and O'Connell, J. (2021). Intrinsic Metallicity Variation in the Intermediate Mass Type II Globular Cluster NGC 1261. *arXiv e-prints*, page arXiv:2106.15052.

Mucciarelli, A., Lapenna, E., Massari, D., Pancino, E., Stetson, P. B., Ferraro, F. R., Lanzoni, B., and Lardo, C. (2015). A chemical trompe-l'Œil: No iron spread in the globular cluster m22. *The Astrophysical Journal*, 809(2):128.

Mészáros, S., Masseron, T., García-Hernández, D. A., Allende Prieto, C., Beers, T. C., Bizyaev, D., Chojnowski, D., Cohen, R. E., Cunha, K., Dell'Agli, F., and et al. (2020). Homogeneous analysis of globular clusters from the apogee survey with the bacchus code – ii. the southern clusters and overview. *Monthly Notices of the Royal Astronomical Society*, 492(2):1641–1670.

Nardiello, D., Libralato, M., Piotto, G., Anderson, J., Bellini, A., Aparicio, A., Bedin, L. R., Cassisi, S., Granata, V., King, I. R., Lucertini, F., Marino, A. F., Milone, A. P., Ortolani, S., Platais, I., and van der Marel, R. P. (2018). The Hubble Space Telescope UV Legacy Survey of Galactic Globular Clusters – XVII. Public Catalogue Release. *Monthly Notices of the Royal Astronomical Society*, 481(3):3382–3393.

Pilachowski, C., Leep, E. M., Wallerstein, G., and Peterson, R. C. (1982). Abundances of the elements in six stars in the globular cluster M 22. *The Astrophysical Journal*, 263:187–198.

Piotto, G., Milone, A. P., Bedin, L. R., Anderson, J., King, I. R., Marino, A. F., Nardiello, D., Aparicio, A., Barbuy, B., Bellini, A., Brown, T. M., Cassisi, S., Cool, A. M., Cunial, A., Dalessandro, E., D'Antona, F., Ferraro, F. R., Hidalgo, S., Lanzoni, B., Monelli, M., Ortolani, S., Renzini, A., Salaris, M., Sarajedini, A., van der Marel, R. P., Vesperini, E., and Zoccali, M. (2015). THEHUBBLE SPACE TELESCOPEUV LEGACY SURVEY OF GALACTIC GLOBULAR CLUSTERS. i. OVERVIEW OF THE PROJECT AND DETECTION OF MULTIPLE STELLAR POPULATIONS. *The Astronomical Journal*, 149(3):91.

Renzini, A. (2008). Origin of multiple stellar populations in globular clusters and their helium enrichment. *Monthly Notices of the Royal Astronomical Society*, 391(1):354–362.

Renzini, A. and Buzzoni, A. (1986). *Global properties of stellar populations and the spectral evolution of galaxies.*, volume 122, pages 195–231.

Renzini, A., D'Antona, F., Cassisi, S., King, I. R., Milone, A. P., Ventura, P., Anderson, J., Bedin, L. R., Bellini, A., Brown, T. M., Piotto, G., van der Marel, R. P., Barbuy, B., Dalessandro, E., Hidalgo, S., Marino, A. F., Ortolani, S., Salaris, M., and Sarajedini, A. (2015). The Hubble Space TelescopeUV Legacy Survey of Galactic Globular Clusters – V. Constraints on formation scenarios. *Monthly Notices of the Royal Astronomical Society*, 454(4):4197–4207.

Renzini, A. and Voli, M. (1981). Advanced evolutionary stages of intermediate-mass stars. I. Evolution of surface compositions. *Astronomy & Astrophysics*, 500:221–239.

Saito, R. K., Hempel, M., Minniti, D., Lucas, P. W., Rejkuba, M., Toledo, I., Gonzalez, O. A., Alonso-García, J., Irwin, M. J., Gonzalez-Solares, E., Hodgkin, S. T., Lewis, J. R., Cross, N., Ivanov, V. D., Kerins, E., Emerson, J. P., Soto, M., Amôres, E. B., Gurovich, S., Dékány, I., Angeloni, R., Beamin, J. C., Catelan, M., Padilla, N., Zoccali, M., Pietrukowicz, P., Moni Bidin, C., Mauro, F., Geisler, D., Folkes, S. L., Sale, S. E., Borissova, J., Kurtev, R., Ahumada, A. V., Alonso, M. V., Adamson, A., Arias, J. I., Bandyopadhyay, R. M., Barbá, R. H., Barbuy, B., Baume, G. L., Bedin, L. R., Bellini, A., Benjamin, R., Bica, E., Bonatto, C., Bronfman, L., Carraro, G., Chenè, A. N., Clariá, J. J., Clarke, J. R. A., Contreras, C., Corvillón, A., de Grijs, R., Dias, B., Drew, J. E., Fariña, C., Feinstein, C., Fernández-Lajús, E., Gamen, R. C., Gieren, W., Goldman, B., González-Fernández, C., Grand, R. J. J., Gunthardt, G., Hambly, N. C., Hanson, M. M., Helminiak, K. G., Hoare, M. G., Huckvale, L., Jordán, A., Kinemuchi, K., Longmore, A., López-Corredoira, M., Maccarone, T., Majaess, D., Martín, E. L., Masetti, N., Mennickent, R. E., Mirabel, I. F., Monaco, L., Morelli, L., Motta, V., Palma, T., Parisi, M. C., Parker, Q., Peñaloza, F., Pietrzy´nski, G., Pignata, G., Popescu, B., Read, M. A., Rojas, A., Roman-Lopes, A., Ruiz, M. T., Saviane, I., Schreiber, M. R., Schröder, A. C., Sharma, S., Smith, M. D., Sodré, L., Stead, J., Stephens, A. W., Tamura, M., Tappert, C., Thompson, M. A., Valenti, E., Vanzi, L., Walton, N. A., Weidmann, W., and Zijlstra, A. (2012). Vvv dr1: The first data release of the milky way bulge and southern plane from the near-infrared eso public survey vista variables in the vía láctea. *Astronomy& Astrophysics*, 537:A107.

Salaris, M., Chieffi, A., and Straniero, O. (1993). The alpha -enhanced Isochrones and Their Impact on the FITS to the Galactic Globular Cluster System. *The Astronomical Journal*, 414:580.

Smith, G. H. and Norris, J. (1982). Comments on the origin of the carbon and nitrogen variations whitin NGC 6752 and 47 Tucanae. *The Astrophysical Journal*, 254:594–605.

Sneden, C. (1973). The nitrogen abundance of the very metal-poor star HD 122563. *The Astronomical Journal*, 184:839.

Thoul, Jorissen, A., Goriely, S., Jehin, E., Magain, P., Noels, A., and Parmentier, G. (2002). Accretion of gas by globular cluster stars. *Astronomy & Astrophysics*, 383(2):491–501.

Vasiliev, E. and Baumgardt, H. (2021). Gaia edr3 view on galactic globular clusters.

Ventura, P. and D'Antona, F. (2009). Massive AGB models of low metallicity: the implications for the self-enrichment scenario in metal-poor globular clusters. *Astronomy & Astrophysics*, 499(3):835–846.

Ventura, P., D'Antona, F., and Mazzitelli, I. (2002). Yields from low metallicity, intermediate mass AGB stars:. Their role for the CNO and lithium abundances in Globular Cluster stars. *Astronomy & Astrophysics*, 393:215–223.

Villanova, S., Geisler, D., Carraro, G., Bidin, C., and Muñoz, C. (2013). Ruprecht 106: the first single population globular cluster? *The Astrophysical Journal*, 778.

Willman, B. and Strader, J. (2012). "galaxy," defined. *The Astronomical Journal*, 144(3):76.

Worley, C. and Cottrell, P. (2010). Heavy element abundances in low gravity globular cluster stars: Ngc 362 and ngc 6388. *Monthly Notices of the Royal Astronomical Society*, 406:2504 – 2520.